https://doi.org/10.5194/egusphere-2026-6714
Preprint. Discussion started: 17 November 2026
© Author(s) 2026. CC BY 4.0 License.

Joint Inversion of Summertime Anthropogenic and Biogenic NO_x and NMVOC Emissions over the Continental United States Using TEMPO and TROPOMI Observations

Chia-Hua Hsu[1,2,3], Daven K. Henze[1], Arthur P. Mizzi[4,5,1], Congmeng Lyu[2,3], Rebecca H. Schwantes[3], Owen R. Cooper[3], Colin Harkins[2,3], Jian He[2,3], Meng Li[2,3], Dylan B. Millet[6], Kelley C. Wells[6], Jennifer Kaiser[7,8], Kelvin H. Bates[1], Shobha Kondragunta[9], R. Bradley Pierce[10], Colby B. Francoeur[1,2,3], Siyuan Wang[11], Gonzalo González Abad[12], Caroline R. Nowlan[12], Xiong Liu[12], Prajjwal Rawat[13,14], Carsten Warneke[3], Matthew M. Coggon[3], Chelsea E. Stockwell[3], Jeff Peischl[3], Nell B. Schafer[2,3,15], Kristen Zuraski[2,3*], Andrew D. Rollins[3], Eleanor M. Waxman[3], Lu Xu[16], Zigang Wei[9], and Brian C. McDonald[3]

[1]Department of Mechanical Engineering, University of Colorado, Boulder, CO, USA
[2]Cooperative Institute for Research in Environmental Sciences, University of Colorado, Boulder, CO, USA
[3]NOAA Chemical Sciences Laboratory, Boulder, CO, USA
[4] NASA Earth Exchange, NASA Ames Research Center, Moffett Field, CA, USA
[5]Bay Area Environmental Research Institute, Moffett Field, CA, USA
[6]Department of Soil, Water, and Climate, University of Minnesota, St. Paul, MN, USA
[7]School of Civil and Environmental Engineering, Georgia Institute of Technology, Atlanta, GA, USA
[8]School of Earth and Atmospheric Sciences, Georgia Institute of Technology, Atlanta, GA, USA
[9]NOAA/NESDIS/Center for Satellite Applications and Research, College Park, MD, USA
[10]Space Science and Engineering Center, University of Wisconsin-Madison, Madison, WI, USA
[11]Rosenstiel School of Marine, Atmospheric, and Earth Science, University of Miami, Miami, FL, USA
[12]Atomic and Molecular Physics Division, Center for Astrophysics | Harvard & Smithsonian, Cambridge, MA, USA
[13]Hampton University, Hampton, VA, USA
[14]NASA Langley Research Center, Hampton, VA, USA
[15]Department of Chemistry, University of Colorado Boulder, Boulder, CO, USA
[16]Department of Energy, Environmental and Chemical Engineering, Washington University in St. Louis, St. Louis, MO, USA
*now at Google Quantum AI, Boulder, CO USA

Corresponding author: Chia-Hua Hsu (Chia-Hua.Hsu@colorado.edu)

https://doi.org/10.5194/egusphere-2026-6714
Preprint. Discussion started: 17 November 2026
© Author(s) 2026. CC BY 4.0 License.



Abstract

Nitrogen oxides (NO_x) and non-methane volatile organic compounds (NMVOCs) are major air pollutants and key precursors to tropospheric ozone. We constrain summertime US NO_x and NMVOC emissions by assimilating midday TEMPO and TROPOMI nitrogen dioxide (NO_2) and formaldehyde (HCHO) observations to assess how joint emission inversions and daytime TEMPO observations improve top-down emission estimates. Satellite NO_2 and HCHO retrievals evaluated against Pandora show negative biases; notably, TROPOMI HCHO is systematically lower than TEMPO HCHO by 30–40% over the southeastern US, and a bias correction was applied to TROPOMI HCHO. Top-down NO_x emissions derived from TEMPO and TROPOMI are 5–20% lower than prior estimates. Posterior biogenic NMVOC emissions are reduced by 40–50%, and top-down anthropogenic NMVOC emissions derived from both satellite datasets are also 20–40% lower in urban areas. While overall top-down NO_x emissions appear underestimated, TEMPO-derived emissions demonstrate better performance than TROPOMI-derived emissions. Updated NMVOC emissions mitigate the prior model overprediction of HCHO and other NMVOC species, with TEMPO data providing stronger constraints while TROPOMI-derived emissions are overcorrected. Joint NO_x and NMVOC inversions yield the best O_3 simulations compared to NMVOC-only inversions. Furthermore, NMVOC emission estimates are sensitive to the NO_x emission inversion, resulting in a 10% difference in posterior emissions due to complex NO_x–hydroxyl radical (OH)–VOC chemical interactions. Our work demonstrates that TEMPO's better midday retrieval quality provides enhanced constraints for top-down emission estimation compared to TROPOMI, laying the groundwork for diurnal geostationary assimilation while highlighting the critical need for multi-species joint inversions.

https://doi.org/10.5194/egusphere-2026-6714
Preprint. Discussion started: 17 November 2026
© Author(s) 2026. CC BY 4.0 License.

1. Introduction

Nitrogen oxides (NO_x = NO + NO_2) and non-methane volatile organic compounds (NMVOCs) are primary precursors of fine particulate matter (i.e., $PM_{2.5}$) and tropospheric ozone (O_3) (Seinfeld & Pandis, 2016). Exposure to high levels of NO_2, $PM_{2.5}$, and O_3 has severe adverse impacts on human health, contributing significantly to respiratory and cardiovascular diseases, as well as premature mortality (Achakulwisut et al., 2019; Lelieveld et al., 2015; Turner et al., 2016; WHO, 2021). The diverse and dynamically evolving natural and anthropogenic sources of NO_x and NMVOCs pose a persistent challenge for accurate emissions estimation (McDonald et al., 2018; Huber et al., 2026).

Anthropogenic NO_x and NMVOC emissions are typically estimated using bottom-up methodologies. However, the accuracy of this approach is often hindered by outdated emission factors and the incompleteness of local activity data (Janssens-Maenhout et al., 2015; Zheng et al., 2018). Furthermore, the spatiotemporal allocation of bottom-up inventories usually relies on static assumptions or surrogate datasets (e.g., population density, land uses), which introduces additional uncertainties (Geng et al., 2017). The chemical diversity of NMVOC species poses another major hurdle for inventory compilation (Hong et al., 2017). Using a different bottom-up approach, biogenic NMVOC emissions are typically simulated using tools such as the Model of Emissions of Gases and Aerosols from Nature (MEGAN; Guenther et al., 2012) or the Biogenic Emission Inventory System (BEIS; Pierce et al., 1998). These models derive emissions based on plant functional types and environmental drivers, primarily temperature and solar radiation. However, inaccuracies in vegetation distribution, empirical model parameterizations, and modeled responses to environmental stressors like drought can introduce substantial uncertainties (Seco et al., 2022; Jiang et al., 2018). For instance, studies have reported that isoprene emission rates estimated by MEGAN and BEIS can exhibit large discrepancies—often by a factor of two or more—when compared directly to field measurements (DiMaria et al., 2023; Warneke et al., 2010).

Alternatively, a top-down approach can be applied to constrain NO_x and NMVOC emissions using observations and improve our understanding of these complex emission sources. Flux measurements are most ideal for top-down emission estimates, however, such data are scarce, while satellites observations offer the benefit of broad spatial coverage and continuous monitoring that assist in tracking emissions across regional to global scales. Satellite remote sensing of nitrogen dioxide (NO_2) and formaldehyde (HCHO) has been widely used to optimize NO_x and NMVOC emissions, respectively, because HCHO serves as a high-

https://doi.org/10.5194/egusphere-2026-6714
Preprint. Discussion started: 17 November 2026
© Author(s) 2026. CC BY 4.0 License.

yield intermediate product in the atmospheric oxidation of many NMVOC species (Skipper et al., 2025). To date, the majority of satellite-based inverse modeling studies have focused on constraining emissions of a single category, optimizing either NO_x or NMVOCs independently (Chaliyakunnel et al., 2019; Feng et al., 2020; Itahashi et al., 2019; Oomen et al., 2024). However, there has been a growing trend toward simultaneously constraining emissions of multiple interacting species. For example, several studies have utilized concurrent NO_2 and HCHO remote sensing measurements to jointly optimize NO_x and NMVOC emissions (Jung et al., 2022; Moon et al., 2026; Opacka et al., 2025; Souri et al., 2020), while others have simultaneously constrained NO_x, SO_2, and CO emissions (Miyazaki et al., 2020; Qu et al., 2022; Wu et al., 2023). This multi-species inversion framework is critical because NO_x, CO, and NMVOCs interact through highly complex chemical feedbacks, largely governed by the hydroxyl radical (OH) pool. Gaubert et al. (2016) demonstrated that optimizing global CO emissions via MOPITT satellite-detected CO increased posterior CO emissions by 27%, which subsequently depleted atmospheric OH by 5-15%. This lower OH concentration reduced ambient HCHO concentrations by 5-10% and extended the lifetimes of primary NMVOCs like acetylene, ethylene, and ethane. Similarly, the oxidation rates of NMVOCs and their corresponding HCHO yields are governed by ambient NO_x concentrations (Chan Miller et al., 2017; Wolfe et al., 2016). Consequently, constraining NO_x, CO, and NMVOC emissions independently may fall short of capturing these chemical feedbacks, introducing additional uncertainties into top-down emission estimates. These chemical interactions underscore the importance of advancing and evaluating fully coupled multi-species emission inversions.

Beyond chemical complexities, constraining NMVOC emissions using satellite data faces a long-standing obstacle stemming from retrieval data quality. HCHO retrievals from earlier low-Earth orbit (LEO) platforms, such as from the Ozone Monitoring Instrument (OMI) and Ozone Mapping and Profiler Suite (OMPS), suffered from high retrieval noise, usually requiring extensive spatiotemporal averaging (e.g., monthly or seasonal scales) to achieve a better signal-to-noise ratio for emission estimates (Choi et al., 2022; Nowlan et al., 2023). Newer LEO satellite platforms, such as the TROPOspheric Monitoring Instrument (TROPOMI), feature finer spatial resolution and more precise HCHO observations, enabling the derivation of weekly NMVOC emissions (De Smedt et al., 2021; Oomen et al., 2024). More recently, the launch of geostationary (GEO) satellite instruments such as Tropospheric Emissions: Monitoring of Pollution (TEMPO) (Zoogman et al., 2017), Geostationary Environment Monitoring Spectrometer (GEMS) (Kim et al., 2019) and Copernicus Sentinel-4,

https://doi.org/10.5194/egusphere-2026-6714
Preprint. Discussion started: 17 November 2026
© Author(s) 2026. CC BY 4.0 License.

which deliver high-quality NO_2 and HCHO data with unprecedented hourly resolution, offers the potential to capture rapid daily/diurnal chemical transitions and enhance our understanding of highly variable NO_x and NMVOC emissions (Abdi-Oskouei et al., 2026; Sun et al., 2025).

Given the scarcity of joint NO_x and NMVOC emissions inversion studies over the conterminous United States (CONUS) (e.g., Jung et al., 2022), we aim at jointly optimizing NO_x and NMVOC emissions by assimilating multi-constituent (NO_2 and HCHO) observations building on our recent work that focused on single-species emissions inversion using TROPOMI and TEMPO NO_2 (Hsu et al., 2026). By implementing a regional data assimilation (DA) system, we aim to investigate the following key scientific questions: (1) How do geostationary TEMPO data enhance the capabilities of top-down emission constraints compared to LEO TROPOMI data? (2) How does a multi-species emission inversion improve emissions estimates and surface O_3 forecasting performance versus a single-species inversion? (3) What are the impacts of multi-species emissions inversion on quantifying regional NMVOC emissions?

2. Emissions Inversion Approach and Model Configuration

In this section, we introduce the DA system, and the modeling tool used in this work.

2.1 Forecast and Data Assimilation System

We use WRF-Chem/Chem-DART (Hsu et al., 2026; Ma et al., 2019; Mizzi et al., 2016; 2018) as our chemical/meteorological DA and emissions inversion system. WRF-Chem/Chem-DART links the Weather Research and Forecasting model with chemistry (WRF-Chem) (Grell et al., 2005) with Chem-DART – the Data Assimilation Research Testbed (DART) (Anderson et al., 2009; Gharamti et al., 2025) as modified to include regional chemical DA and top-down emissions estimate capabilities (Chem-DART) (Mizzi et al., 2016; 2018). Chem-DART is an ensemble Kalman filter (EnKF)-based data assimilation (DA) system (Mizzi et al., 2016, 2018). The modules of Chem-DART comprise: (1) ensemble perturbation codes for creating meteorological, chemical initial/boundary conditions (ICs/BCs), and emission inputs; (2) forward observation operators for calculating model-equivalent trace gas columns tailored to various satellite instruments (e.g., TEMPO, TROPOMI, and OMI); and (3) an emission adjustment algorithm that propagates emission scaling factors forward in time to facilitate chemical DA and top-down emission inversions.

2.2 WRF-Chem Model Configuration

https://doi.org/10.5194/egusphere-2026-6714
Preprint. Discussion started: 17 November 2026
© Author(s) 2026. CC BY 4.0 License.

We use WRF-Chem version 4.2.2 for chemical weather ensemble forecasts. The model domain covers the CONUS with horizontal resolution of 12 km and 50 vertical layers from the surface to 50 hPa. The physics and chemistry configuration as well as the initial and boundary conditions input follow the setup in Hsu et al. (2026). The major change in this study is the use of a more sophisticated gas-phase chemical mechanism (RACM2B_VCP2, Zhu et al., 2024; Zhu et al., 2025), which is an updated version of the RACM-ESRL-VCP mechanism (Coggon et al., 2021). The RACM2B_VCP2 builds on the RACM2 (Goliff et al., 2013) and RACM2-Berkeley2.0 (Browne et al., 2014 and Zare et al., 2018) mechanisms and accounts for the chemistry from volatile chemical products (Zhu et al., 2024) and cooking sources (Coggon et al., 2024; Zhu et al., 2025). These upgrades to better represent the oxidation products of various NMVOCs are important for accurately representing HCHO production.

The prior anthropogenic emissions over CONUS used in this study are derived from GReenhouse gas And Air Pollutants Emissions System version 1.0 (GRA^{2}PES) (Lyu et al., 2025) developed by the NOAA Chemical Sciences Laboratory. This inventory consists of emissions from various sources including power generation, industrial point sources, mobile, oil & gas production, cooking and volatile consumer products (He et al., 2023; McDonald et al., 2018). The anthropogenic NO_x and NMVOC emissions were estimated based on activity data corresponding to the year 2023 (He et al., 2023). Anthropogenic emissions in Canada and Mexico are derived from the Copernicus Atmospheric Monitoring Service version 4.2 (Doumbia et al., 2021). The fire emissions used in this study are calculated by combining fire radiative power (FRP) data from the Regional hourly ABI and VIIRS Emissions (RAVE) product (Li et al., 2022) with smoke emission factors derived from the 2019 Fire Influence on Regional to Global Environments and Air Quality (FIREX-AQ) field campaign (Stockwell et al., 2022). The biogenic NMVOC emissions and soil NO are calculated online using BEIS3.14 (Pierce et al., 1998; Bash et al., 2016) in WRF-Chem (bio_emiss_opt =3), with the biogenic NMVOC emissions computed following Eq (1).

$$e_{b,actual} = e_{b,ref} \times c_T \times c_L \quad (1)$$

Where $e_{b,actual}$ and $e_{b,ref}$ represent the actual and input reference biogenic emissions (mole km^{-2} hr^{-1}), and the c_T and c_L are the temperature and light correction factors, which are calculated from the meteorological fields within WRF. The reference biogenic isoprene emissions include updates to urban vegetation described in Zhu et al. (2024) and are reduced

https://doi.org/10.5194/egusphere-2026-6714
Preprint. Discussion started: 17 November 2026
© Author(s) 2026. CC BY 4.0 License.

by 25% following He et al. (2023), as unscaled input tends to overestimate isoprene emissions. The anthropogenic NO_x and NMVOC emissions and the reference biogenic emissions are constrained by the satellite NO_2 and HCHO columns through the DA process. A comprehensive list of model configurations and input data information is provided in Table S1.

2.3 Joint NMVOC and NO_x Emissions Inversion Algorithms

The DA and emissions inversion is achieved by solving the Kalman filter equations, which derive an optimal solution by blending information from observations and prior constraints (Houtekamer & Zhang, 2016):

$$x_a = x_f + K\left(y - Hx_f\right) \tag{2}$$

$$P_a = (I - KH)P_f \tag{3}$$

$$K = P_f H^T \left(HP_f H^T + R\right)^{-1} \tag{4}$$

Where x represents the state vector, P denotes the background error covariance matrix, K is the Kalman gain matrix, y is the observation vector, H represents the observation operator, and R is the observation error covariance matrix. The subscripts "a" and "f" denote the analysis (posterior) and forecast (prior) states, respectively. In our work, the state vector encompasses model meteorology variables (wind fields, temperature, and moisture), trace gases mixing ratio, and emissions. The background error covariance matrix P_f, is estimated from the WRF-Chem forecast ensemble as:

$$P_f = \frac{1}{m-1} \sum_{i=1}^{m} \left(x_f^i - \overline{x_f}\right)\left(x_f^i - \overline{x_f}\right)^T \tag{5}$$

where x_f^i and $\overline{x_f}$ denote the i-th ensemble member and the ensemble mean of the forecast state vector, respectively, and m represents the ensemble size. Because P_f is directly propagated by the WRF-Chem ensemble, its spatiotemporal covariance structure evolves dynamically with the model physics and chemistry, providing a flow-dependent background error covariance (Houtekamer & Zhang, 2016). P_f also plays a key role in linking observations to model state variables and determining the spatial correction patterns when observations are assimilated. Several analysis schemes (Tippett et al., 2003) have been developed to solve this optimization problem, and the Ensemble Adjustment Kalman Filter (EAKF; Anderson, 2001, 2003) is used

https://doi.org/10.5194/egusphere-2026-6714
Preprint. Discussion started: 17 November 2026
© Author(s) 2026. CC BY 4.0 License.

in this study. The detailed implementation of the EAKF for updating emissions is described in Hsu et al. (2026). Here, we briefly outline the workflow of our emissions inversion and explain how the various NMVOC emission species are constrained.

The joint NO_x and NMVOC emission inversion begins with a WRF-Chem ensemble forecast. We employ a 20-member ensemble with a 3-hour DA cycle (00, 03, ..., and 21 UTC). The WRF-Chem ensemble forecast starts on August 7, 2023 at 00 UTC, building on a deterministic WRF-Chem spin-up simulation initialized on July 21, 2023 at 00 UTC to ensure that meteorological and chemical fields are fully spun up before ensemble generation. The ensemble is initialized by imposing spatiotemporally correlated Gaussian perturbations with a 30% standard deviation on the prior emissions and the chemical IC/BCs. This 30% uncertainty is consistent with reported uncertainties in bottom-up emission inventories and regional chemical boundary forcing (e.g., Miyazaki et al., 2017; McDonald et al., 2018; Solazzo et al., 2017; Travis et al., 2016). During the assimilation process, the Gaspari-Cohn (GC) localization function (Gaspari & Cohn, 1999) is applied to suppress spurious ensemble correlations between distant state variables and observations. Vertical localization is disabled for both NO_2 and HCHO column measurements. The horizontal localization half-width for NO_2 is set to approximately 38 km based on sensitivity experiments evaluating different localization length scales for NO_2 data assimilation. This same localization radius is also applied to HCHO observations to account for its short chemical lifetime. The vertical and horizontal localization half-widths for meteorological observations are set to 1 km and 150 km, respectively. We also apply variable localization (Kang et al., 2011), which restricts NO_2 column measurements to updating only NO_x mixing ratios and emissions. Similarly, HCHO column observations only update model HCHO mixing ratios and anthropogenic/biogenic NMVOC emissions, while meteorological observations solely update their corresponding physical state variables (e.g., temperature, moisture, pressure, and wind fields). Hourly NO_x and NMVOC emissions are dynamically updated during the analysis time when daytime TEMPO and TROPOMI observations are available. For non-analysis hours or during the night, emissions scaling factors—defined as the ratio of posterior to prior emissions at the previous analysis time for each grid cell—are applied to scale emissions forward in time. The underlying assumption is that prior emission errors are mainly systematic, meaning the corrections derived during daytime assimilation cycles can be seamlessly applied to subsequent hours. A more comprehensive description of this emissions adjustment scheme is provided in Hsu et al. (2024), and the detailed configurations of the DA system are summarized in Table S1.

https://doi.org/10.5194/egusphere-2026-6714
Preprint. Discussion started: 17 November 2026
© Author(s) 2026. CC BY 4.0 License.

To date, the majority of NMVOC emission inversion studies have sought to constrain total or sector-aggregated emissions—such as biogenic, anthropogenic, and biomass burning sources (e.g., Oomen et al., 2024; Fang et al., 2024; Bauwens et al., 2016; Souri et al., 2020; Stavrakou et al., 2009)—while only a few studies have endeavored to explicitly optimize individual NMVOC species (e.g., Cao et al., 2018; Choi et al., 2022). Given that new GEO platforms provide spatiotemporally dense HCHO measurements, offering opportunities to better resolve the complex composition of NMVOC emissions, we aggregate individual NMVOC species based on their chemical properties prior to optimization. Specifically, anthropogenic NMVOC emissions are lumped into seven chemical groups—alkanes, alkenes, aldehydes, alcohols, aromatics, ketones, and other NMVOCs—each of which is constrained separately. Biogenic isoprene emissions are constrained directly because they constitute the dominant fraction of biogenic NMVOC emissions, whereas all other biogenic NMVOC species are lumped and optimized together. This lumping strategy is motivated by the distinct HCHO production yields across different NMVOC precursor groups, as demonstrated by Skipper et al. (2024), while effectively reducing the NMVOC emission component of the state vector to nine elements. Table S2 summarizes the specific NMVOC emission species and groups constrained in this study. Individual NMVOC species within an aggregated group are adjusted using a scaling factor derived from the ratio of the posterior to prior emissions of that lumped group; a detailed example demonstrating this approach is provided in Text S1.

3 Data

3.1 Ground-Based and Airborne Observations

Ground-based Pandora spectrometer measurements of NO_2 and HCHO columns are used to assess the accuracy of the TEMPO and TROPOMI satellite observations. The Pandora instrument is a hyperspectral UV–visible spectrometer (Herman et al., 2009; Spinei et al., 2018) designed to provide high-precision measurements of trace gases. In this study, we utilize direct-sun mode data obtained via the Pandonia Global Network (PGN) website (https://www.pandonia-global-network.org/, last accessed: Dec 1, 2025).

The performance of the joint NO_x and NMVOC emission inversion is evaluated by comparing the WRF-Chem simulations against three in situ measurement datasets: (1) surface observations of O_3 and NO_2 from the US EPA Air Quality System (AQS; https://aqs.epa.gov/aqsweb/airdata/download_files.html), with sites mapped in Figure S1, (2) four surface HCHO monitoring sites located in Atlanta, Georgia and across the northeastern

https://doi.org/10.5194/egusphere-2026-6714
Preprint. Discussion started: 17 November 2026
© Author(s) 2026. CC BY 4.0 License.

US, and (3) airborne measurements of O_3, NO_x, and NMVOCs collected during the Atmospheric Emissions and Reactions Observed from Megacities to Marine Areas (AEROMMA; https://csl.noaa.gov/projects/aeromma/data.html) field campaign (Chace et al., 2025).

During the AEROMMA field campaign, a diverse suite of trace gas and aerosol species was measured by instruments onboard the NASA DC-8 research aircraft. The DC-8 aircraft sampled air quality in the boundary layer over major urban areas, including New York City (NYC), Chicago, Los Angeles (LA), and Toronto, with a total of eight flights utilized in this study. The final DC-8 in situ data are aggregated to a 1-minute temporal resolution for direct comparison with the model output. More detailed information regarding the surface HCHO and DC-8 measurements used in this study is summarized in Table 1.

Table 1. HCHO and DC-8 data used in this study.

HCHO measurement		
Site Location [lat, lon]	Instrument	Notes and Reference
Westport, CT [41.12, -73.34]	Aerodyne TILDAS	
Flax Pond, NY [40.96, -73.14]	Aerodyne TILDAS	
New Brunswick, NJ [40.46, -74.43]	Picarro G2307	
South Dekalb, GA [33.69, -84.29]	Picarro G2307	Mouat, Siegel, and Kaiser (2024)
DC-8 measurement		
Chemical Species	Instrument	Notes and Reference
NO & NO_2	laser induced fluorescence (LIF)	Rollins et al. (2020); Waxman et al. (2025)
O_3	NO-induced chemiluminescence	Bourgeois et al. (2020)
HCHO	In Situ Airborne Formaldehyde (ISAF)	Cazorla et al. (2015)
Ethane	Quantum Cascade Tunable Infrared Laser Differential Absorption Spectrometer (QC-TILDAS)	Knighton et al. (2012)
Glyoxal	Airborne Cavity Enhanced Spectrometer (ACES)	Min et al. (2016)
Other NMVOC*	Proton-Transfer Reaction Time-of-Flight Mass Spectrometry (PTR-ToF-MS)	Yuan et al. (2016)

https://doi.org/10.5194/egusphere-2026-6714
Preprint. Discussion started: 17 November 2026
© Author(s) 2026. CC BY 4.0 License.

*Measurements for methanol, ethanol, isoprene, sum of methyl vinyl ketone and methacrolein (MVKMAC), benzene, toluene, and total monoterpenes are used.

3.2 TEMPO/TROPOMI HCHO and NO_2 Retrievals

TEMPO and TROPOMI are space-borne spectrometers that measure atmospheric composition, including NO_2, O_3, and HCHO, using solar backscattered radiation. The TROPOMI instrument operates in a sun-synchronous low Earth orbit, with a daily equatorial overpass at approximately 13:30 local solar time. Its pixel dimensions at nadir were originally 3.5 x 7 km² and were reduced to 3.5 x 5.6 km² on August 6, 2019. TROPOMI provides global coverage within a single day. In contrast, TEMPO is positioned in a geostationary orbit at 91.0° W longitude, with a Field of Regard (FoR) focusing on North America. TEMPO began collecting observations in August 2023 with a native pixel resolution of 2 x 4.75 km² at the center of its FoR and performs mostly hourly measurements throughout local daytime.

Both TEMPO and TROPOMI detect NO_2 and HCHO in the ultraviolet-visible spectrum. The abundances of NO_2 and HCHO are retrieved by analyzing trace gas light absorption at specific wavelengths using the differential optical absorption spectroscopy (DOAS) method or a similar approach of direct fitting of the radiance spectrum (TEMPO) to derive the total slant column density (SCD) of NO_2 and HCHO along the optical light path from the surface to the satellite instrument. These satellite SCDs are subsequently converted to vertical column densities (VCDs) using air mass factors (AMFs), which are derived from altitude-dependent scattering weights (i.e., box AMF) calculated by a radiative transfer model and a priori NO_2 and HCHO vertical profiles obtained from a chemical transport model. In the case of NO_2, an additional step separates the tropospheric and stratospheric vertical column densities. Complete descriptions of the NO_2 and HCHO retrieval algorithms are provided by Nowlan et al. (2025) and González Abad et al. (2025) for TEMPO, and Van Geffen et al. (2022b) and De Smedt et al. (2018) for TROPOMI.

We use tropospheric NO_2 SCD and HCHO VCD from the TROPOMI version 2.5 offline level 2 product (Copernicus Sentinel-5P, 2020, 2021) and TEMPO version 4 (V04) level 2 product for NO_x and NMVOC (Liu, 2026a, 2026b) emissions inversion. The satellite tropospheric NO_2 SCDs are calculated by multiplying the tropospheric NO_2 VCDs by the reported tropospheric AMFs. For data quality control, TROPOMI data are filtered to include only pixels with a quality assurance flag exceeding 0.75. For TEMPO, observations are selected based on a main quality flag of 0, an effective cloud fraction below 0.1, and a solar zenith angle of less than 70 degrees. Furthermore, we exclude both TROPOMI and TEMPO

https://doi.org/10.5194/egusphere-2026-6714
Preprint. Discussion started: 17 November 2026
© Author(s) 2026. CC BY 4.0 License.

NO_2 and HCHO data over water bodies (e.g., oceans and lakes), as our focus is on constraining emission sources over land. Observations over the lakes were excluded because the WRF-Chem simulation underestimated the planetary boundary layer height over water, resulting in an overestimation of simulated NO_2 that could compromise the accuracy of emission inversions for adjacent cities (Hsu et al., 2026).

Figure 1 shows the spatiotemporally averaged TEMPO and TROPOMI NO_2 and HCHO columns for August 7–26, 2023. TEMPO data were unavailable on August 10, 13–14, and 24 during this early operational phase, so TROPOMI data for those dates were omitted for consistency. Both datasets are spatially aggregated to the WRF-Chem model resolution (12 km × 12 km). For this comparison, we only use TEMPO observations from 18 and 21 UTC (corresponding to 10-13 and 13-16 LST) to constrain the emission inversion (Section 5), whereas all available TROPOMI overpass data (corresponding to ~12-14 LST) are included. For NO_2 SCDs (Figure 1a & 1b), both instruments show strong spatial agreement, capturing major NO_2 hotspots over urban areas within the CONUS, sharp gradients between rural and urban regions, and elevated NO_2 levels over the Permian Basin in western Texas, a prominent oil and gas production region.

To account for the differing vertical sensitivities of the two satellite instruments, a forward WRF-Chem simulation—configured as described in Section 2.2—is used as an intercomparison platform (Zhang et al., 2010; Hsu et al., 2026). The difference between TROPOMI and TEMPO columns, $\Delta\Omega$, is then defined as:

$$\Delta\Omega = \left(\Omega_{TEMPO} - \Omega_{TEMPO,M}\right) - \left(\Omega_{TROPOMI} - \Omega_{TROPOMI,M}\right) \quad (6)$$

The terms Ω_{TEMPO} ($\Omega_{TROPOMI}$) and $\Omega_{TEMPO,M}$($\Omega_{TROPOMI,M}$) represent the observed TEMPO (TROPOMI) NO_2 SCDs (or HCHO VCDs) and their corresponding WRF-Chem simulated counterpart after applying each instrument's respective averaging kernel. The differences between TROPOMI and TEMPO NO_2 SCDs are primarily within $\pm 5\times10^{14}$ molec cm^{-2} (Figure 1c), although TROPOMI tends to report higher NO_2 levels in rural and remote regions compared to TEMPO.

In contrast, TEMPO and TROPOMI HCHO observations exhibit larger discrepancies, as illustrated in Figures 1d to 1f. Although both instruments capture enhanced HCHO columns over the southeastern US driven by intense biogenic NMVOC emissions (Kaiser et al., 2018; Mao et al., 2018), the TROPOMI HCHO VCDs are 20–40% lower than the TEMPO values

https://doi.org/10.5194/egusphere-2026-6714
Preprint. Discussion started: 17 November 2026
© Author(s) 2026. CC BY 4.0 License.

across southern latitudes extending up into the Midwest (Figure 1f). Additionally, the TROPOMI HCHO data are noisier than the TEMPO data, indicating a better signal-to-noise ratio in the TEMPO HCHO retrievals.

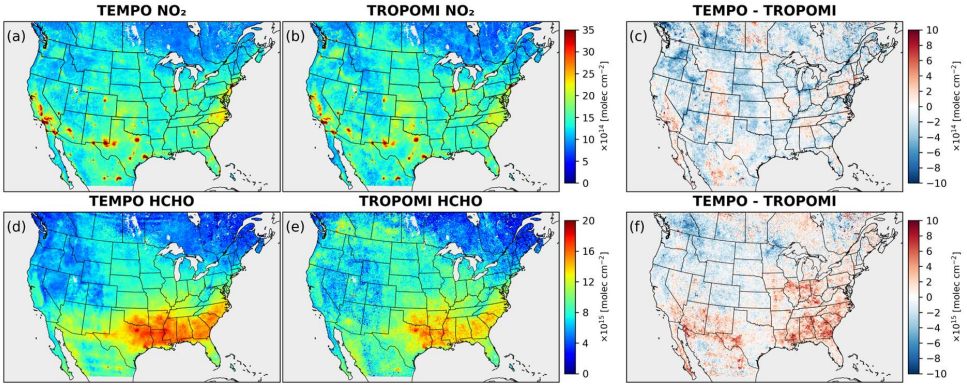


Figure 1. Spatiotemporally averaged TEMPO and TROPOMI NO_2 and HCHO columns and their comparison for August 7–26, 2023. (a) TEMPO NO_2 tropospheric SCD, (b) TROPOMI NO_2 tropospheric SCD, (c) TEMPO minus TROPOMI NO_2 SCD, (d) TEMPO HCHO VCD, (e) TROPOMI HCHO VCD, and (f) TEMPO minus TROPOMI HCHO VCD.

3.3. CrIS Isoprene Column

Isoprene total column retrievals (Wells et al., 2020, 2022) from the Cross-track Infrared Sounder (CrIS) are used to evaluate the top-down biogenic isoprene emissions, owing to the scarcity of in situ NMVOC observations. The retrieval is derived using the Retrieval of Organics from CrIS Radiances (ROCR), an algorithm that uses a machine learning framework to quantify isoprene column abundance from the measured hyperspectral range index (HRI; Walker et al., 2011). For a detailed review of the algorithm, see Wells et al. (2022). Global isoprene column data are available from the CrIS instruments onboard the Suomi National Polar-orbiting Partnership (Suomi-NPP; launched October 2011), NOAA-20 (launched November 2017), and NOAA-21 (launched November 2022) platforms at a spatial resolution of 0.5° × 0.625°, aggregated from the native CrIS footprint resolution (~14 km at nadir) to increase the signal-to-noise. In this study, the August 2023 isoprene column data are obtained from the NOAA-21 CrIS sensor.

3.4 Meteorological Observations

https://doi.org/10.5194/egusphere-2026-6714
Preprint. Discussion started: 17 November 2026
© Author(s) 2026. CC BY 4.0 License.

The meteorological observations dataset is obtained from NCEP ADP Global Upper Air and Surface Weather Observations (https://rda.ucar.edu/datasets/d337000/) which consist of observations from the surface network, radiosondes, the Aircraft Communications and Reporting System, and satellite-derived winds. These measurements are assimilated to constrain our WRF-Chem meteorological simulation.

4. Evaluation of TEMPO/TROPOMI HCHO & NO_2 Column Measurements

As the data quality of satellite NO_2 and HCHO columns directly influences top-down emissions estimates, we utilize Pandora measurements to evaluate the accuracy and potential systematic bias of NO_2 and HCHO data from TROPOMI and TEMPO prior to performing emissions inversion. Pandora direct-sun mode provides high-precision column observations with minimal radiative transfer assumptions, serving as an established benchmark for satellite data evaluation (Chi et al., 2025; Herman et al., 2009; Spinei et al., 2018; Verhoelst et al., 2021). We collect Pandora data within our WRF-Chem domain from August 1 to 31, 2023 for analysis. Rather than directly comparing satellite columns to Pandora observations, we adopt the methodology of Hsu et al. (2026) and use WRF-Chem model outputs as a transfer platform to properly account for the differing vertical sensitivities of the satellite sensors. The discrepancy between the satellite and Pandora columns is computed as follows:

$$\Delta\Omega = \left(\Omega_{SAT} - \Omega_{SAT,M}\right) - \left(\Omega_{PAN} - \Omega_{PAN,M}\right) \quad (7)$$

Where $\Delta\Omega$ represents the final difference between satellite and Pandora columns. The terms Ω_{SAT} and $\Omega_{SAT,M}$ denote the retrieved satellite column and its corresponding WRF-Chem simulated counterpart after applying the satellite's averaging kernel. Similarly, Ω_{PAN} and $\Omega_{PAN,M}$ represent the measured Pandora column and its corresponding WRF-Chem simulated value, with the latter calculated via a simple vertical summation of the modeled trace gas partial columns at the Pandora site locations.

For Pandora NO_2, only high-quality measurements with a quality flag of 0 or 10 are retained. We derive the tropospheric NO_2 component by subtracting the collocated satellite stratospheric column (provided by the respective TEMPO and TROPOMI products) from the Pandora total NO_2 column, following Judd et al. (2020). The spatiotemporal collocation criteria for pairing Pandora and satellite NO_2 observations are defined as follows: (1) all Pandora measurements within ±10 minutes of the satellite overpass are averaged for comparison with

https://doi.org/10.5194/egusphere-2026-6714
Preprint. Discussion started: 17 November 2026
© Author(s) 2026. CC BY 4.0 License.

the satellite pixel; (2) the center of the collocated satellite ground pixel must be within 5 km of the Pandora site; and (3) satellite observations must pass the data screening described in Section 3.2. For Pandora HCHO data, an alternative filtering approach is applied following Rawat et al. (2025). Briefly, reliable Pandora sites for HCHO measurements are first identified by verifying good agreement between sky-scan and direct-sun mode observations. Subsequently, the reported independent uncertainty and weighted root mean square (wrms) are used for data screening rather than the standard quality flags. This approach substantially increases the volume of usable Pandora HCHO data compared to strict quality-flag filtering. The spatiotemporal collocation criteria for HCHO match those used for NO_2, and the Pandora sites utilized in this study are listed in Table S3.

Figure 2 presents the comparison between satellite tropospheric NO_2 VCDs and the Pandora data. The mean difference for each site is shown, displaying the satellite bias as a function of the satellite NO_2 column abundance. To examine the diurnal variation in TEMPO data quality, the evaluation is partitioned into morning (07–12 Local Standard Time (LST)), midday (12–15 LST), and late afternoon (15–18 LST) intervals. Both TEMPO and TROPOMI tropospheric NO_2 VCDs exhibit similar bias patterns, underestimating column abundances relative to Pandora measurements, particularly under high-NO_2 conditions such as urban areas. Based on ordinary least squares regression slopes, the satellite retrievals exhibit a negative bias of 19% to 35% in August 2023. While TROPOMI and midday TEMPO observations show comparable and smaller bias magnitudes, TEMPO NO_2 retrievals during non-midday hours tend to display larger negative biases.

Figure 3 illustrates the comparison between satellite HCHO VCDs and Pandora observations. Similar to the NO_2 results, TEMPO HCHO retrievals are biased low relative to Pandora data. However, midday observations (Figure 3b) tend to show a smaller underestimation (-14%) compared to those in the morning (-23%) and late afternoon (-17%). The TROPOMI HCHO VCD bias pattern resembles that of midday TEMPO data, with negative bias of -19% (Figure 3d). This TROPOMI HCHO evaluation aligns with previous studies utilizing ground-based Fourier-transform infrared (FTIR) spectrometers; for instance, Vigouroux et al. (2020) and Oomen et al. (2024) reported that TROPOMI HCHO columns are biased low by 30–50% in regions characterized by high HCHO VCDs.

Our analysis demonstrates that TEMPO NO_2 and HCHO retrievals share a similar bias pattern, with both satellite columns exhibiting systematic low biases relative to Pandora observations. Because this comparison is based on a single month of data, the observed bias

https://doi.org/10.5194/egusphere-2026-6714
Preprint. Discussion started: 17 November 2026
© Author(s) 2026. CC BY 4.0 License.

patterns may differ when evaluated over longer-term periods. This highlights the need for further investigation into satellite retrieval algorithms to pinpoint the root causes of these discrepancies and better understand potential diurnal variations in bias, particularly in TEMPO V04 data. Potential contributing factors include reduced vertical sensitivity in the lower troposphere at high solar zenith angles or systematic uncertainties in air mass factor (AMF) calculations (Beaudry & Cohen, 2026). For a more comprehensive, long-term evaluation of TEMPO V03 NO_2 and HCHO columns against Pandora network data, see Ghahremanloo et al. (2025), Rawat et al. (2026) and Ortega et al. (2026).

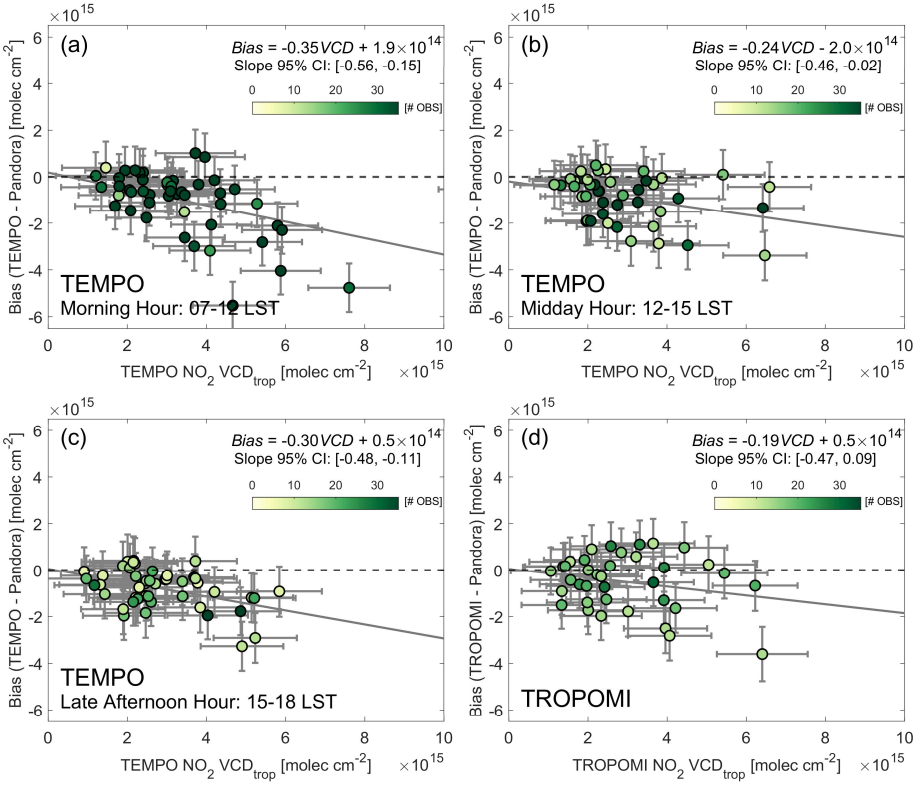


Figure 2. Comparison of satellite and Pandora NO_2 VCDs: (a) TEMPO morning (07–12 LST), (b) TEMPO midday (12–15 LST), (c) TEMPO late afternoon (15–18 LST), and (d) TROPOMI (12–14 LST). The linear regression line is shown in grey. Color shading indicates the number of paired Pandora and satellite observations. Error bars represent the uncertainties of the biases and satellite NO_2 columns, calculated via error propagation from the reported uncertainties of the satellite retrievals and Pandora measurements, along with a systematic error term of 10^{15}

https://doi.org/10.5194/egusphere-2026-6714
Preprint. Discussion started: 17 November 2026
© Author(s) 2026. CC BY 4.0 License.

molec cm^{-2} following Hsu et al. (2026). The 95% confidence interval (CI) of the regression slope is also shown.

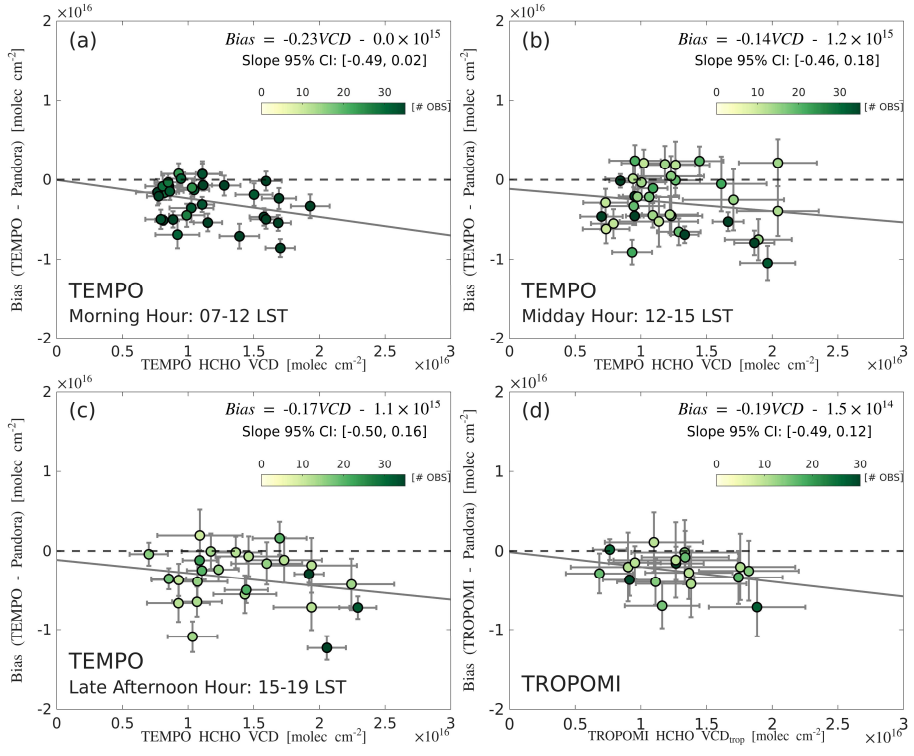


Figure 3. Comparison of satellite and Pandora HCHO VCDs: (a) TEMPO morning (07–12 LST), (b) TEMPO midday (12–15 LST), (c) TEMPO late afternoon (15–18 LST), and (d) TROPOMI (12–14 LST). The linear regression line is shown in grey. Color shading indicates the number of paired Pandora and satellite observations. Error bars represent the uncertainties of the biases and satellite HCHO columns, calculated via error propagation from the reported uncertainties of the satellite retrievals and Pandora measurements, along with a systematic error term of 10^{15} molec cm^{-2} following Hsu et al. (2026). The 95% confidence interval (CI) of the regression slope is also shown.

4.1 Bias-correction for the satellite data

Given that satellite NO_2 and HCHO retrievals often exhibit systematic biases, applying bias corrections prior to emissions inversion is an important consideration. In this study, we apply a bias correction exclusively to TROPOMI HCHO columns. This is owing to a

https://doi.org/10.5194/egusphere-2026-6714
Preprint. Discussion started: 17 November 2026
© Author(s) 2026. CC BY 4.0 License.

pronounced low bias in TROPOMI HCHO retrievals, that has been well documented in previous evaluation studies (e.g., Vigouroux et al., 2020; De Smedt et al., 2021), and recent inverse modeling works have demonstrated that assimilating uncorrected TROPOMI HCHO columns can lead to systematic underestimations of top-down NMVOC emissions (Fang et al., 2024; Oomen et al., 2024). Furthermore, the notably lower TROPOMI HCHO abundances observed over the southeastern US compared to TEMPO (Figure 1) suggest a substantial regional underestimation that requires correction. Consequently, we correct TROPOMI HCHO VCD based on our ground-based Pandora evaluation in Section 4. The satellite data bias is parameterized as a function of the raw column abundance using the linear regression curve shown in Figure 3d:

$$Bias = -0.19VCD - 1.5 \times 10^{14} \quad (8)$$

where VCD is the raw TROPOMI HCHO column value. The bias-corrected TROPOMI HCHO columns (VCD_{BC}) are subsequently calculated using the following equation:

$$VCD_{BC} = VCD - Bias = 1.19\,VCD + 1.5 \times 10^{14} \quad (9)$$

This linear scaling relationship is applied to the raw TROPOMI HCHO observations prior to DA, yielding an adjustment magnitude consistent with previous inverse modeling studies (Fang et al., 2024; Oomen et al., 2024).

In contrast, satellite NO_2 observations (from both TROPOMI and TEMPO) and TEMPO HCHO data are not corrected in this study. While negative biases in TROPOMI NO_2 retrievals over polluted regions are recognized (Judd et al., 2020; Verhoelst et al., 2021; Lange et al., 2023), widely used bias-correction methods for satellite NO_2 data remain scarce. For the new TEMPO V04 observations, more extensive evaluation analyses are required to thoroughly characterize its bias patterns across different regions and observation hours, which will facilitate the development of a robust bias-correction approach in future work. Moreover, as demonstrated in Sections 6.3 and 7, uncorrected TEMPO midday HCHO observations show promising performance in constraining NMVOC emissions, mitigating the immediate necessity for bias-correction in this work.

5. Experimental design

https://doi.org/10.5194/egusphere-2026-6714
Preprint. Discussion started: 17 November 2026
© Author(s) 2026. CC BY 4.0 License.

We conduct a 21-day simulation spanning August 7–26, 2026, comprising four distinct numerical experiments. The detailed configuration for each run is provided in Table 2. The first experiment is the control run (CTRL), a baseline simulation that constrains only meteorological fields by assimilating observations of pressure, air temperature, wind components, and specific humidity. We use a ±1.5 hour DA window, centered on the analysis hour, to assimilate the meteorological data.

The remaining three experiments assimilate satellite trace gas observations in tandem with the meteorological data to simultaneously update the meteorological, chemical and emission state variables. Satellite NO_2 SCDs are assimilated to minimize the uncertainties associated with AMF calculations derived from a priori NO_2 profiles, while for HCHO, VCDs from both the TEMPO and TROPOMI instruments are utilized to enable a fair intercomparison following the bias correction applied to TROPOMI HCHO VCDs. The TROPOMI experiment (TROPOMI-JOINT) assimilates TROPOMI NO_2 SCDs and HCHO VCDs using a ±1.5-hour DA window. Specifically, HCHO columns are used to constrain anthropogenic and biogenic NMVOC emissions alongside HCHO mixing ratios, whereas NO_2 columns update NO_x emissions and mixing ratios.

For TEMPO observations, we design two experiments (TEMPO-HCHO and TEMPO-JOINT) that employ a narrower DA window (±0.5 hours), which yields superior emission inversion results compared to a wider ±1.5-hour window as reported by Hsu et al. (2024). We employ a 3-hour DA cycle, under which TEMPO observations at 12, 15, 18, 21, and 00 UTC could potentially be assimilated. However, due to potential larger biases in early-morning and late-afternoon TEMPO retrievals (Section 4), assimilation of these non-midday hours has been shown to degrade top-down NO_x emission estimates (Hsu et al., 2026). We therefore assimilate only near-midday TEMPO observations (18 and 21 UTC) following Hsu et al. (2026). The TEMPO-HCHO experiment assimilates solely TEMPO HCHO observations at 18 and 21 UTC (i.e. observations within 30 minutes of these target hours) to optimize NMVOC emissions and HCHO mixing ratios. The TEMPO-JOINT experiment assimilates both TEMPO NO_2 SCDs and HCHO VCDs at these same hours to jointly constrain NO_x and NMVOC emissions along with their associated chemical mixing ratios

A comparison between TEMPO-JOINT and TEMPO-HCHO isolates the benefit of a joint emissions inversion relative to optimizing solely NMVOC emissions, given that NO_x levels substantially modulate NMVOC oxidation pathways and subsequent HCHO yields as well as changing the OH abundance in the atmosphere. Furthermore, comparing TEMPO-JOINT with

https://doi.org/10.5194/egusphere-2026-6714
Preprint. Discussion started: 17 November 2026
© Author(s) 2026. CC BY 4.0 License.

TROPOMI-JOINT enables a direct evaluation of top-down inversion performance when utilizing GEO versus LEO satellite datasets during midday hours.

We aggregate the TROPOMI and TEMPO pixels into super-observations at a 12 × 12 km² resolution to match the WRF-Chem grid prior to DA. This spatial aggregation reduces data volume and mitigates the computational burden of assimilating dense TEMPO data, while simultaneously reducing random noise in the HCHO retrievals. The super-observation columns and their corresponding uncertainties are calculated via simple arithmetic averaging as follows:

$$\overline{\Omega} = \frac{1}{N}\sum_{i=1}^{N} \Omega_i \quad (10)$$

$$\overline{\sigma} = \frac{1}{N}\sqrt{\sum_{i=1}^{N} \sigma_i^2} \quad (11)$$

Where $\overline{\Omega}$, and $\overline{\sigma}$ are the aggregated column value and its associated uncertainty, while N represents the total number of pixel centers located within a given WRF-Chem grid cell. The terms Ω_i and σ_i are the original column value and uncertainty for each individual pixel provided from the retrieval product. Typically, a single WRF-Chem grid cell encompasses approximately 10–12 TEMPO pixels or 5–7 TROPOMI pixels.

Table 2. Experimental design for emissions inversion and total number of super-observations assimilated in the experiment.

Experiment	MET (CHEM) DA window (hours)	OBS being assimilated	# of NO_2 (HCHO) OBS
CTRL	±1.5 (NA)	Meteorological (MET) data	N/A
TROPOMI-JOINT*	±1.5 (±1.5)	MET + TROPOMI NO_2 SCDs & HCHO VCDs (all scans)	1,029,088 (967,426)
TEMPO-HCHO	±1.5 (±0.5)	MET + TEMPO HCHO VCDs (18 & 21 UTC)	N/A (1,578,523)
TEMPO-JOINT	±1.5 (±0.5)	MET + TEMPO NO_2 SCDs & HCHO VCDs (18, 21 UTC)	1,542,779 (1,578,523)

* The TROPOMI HCHO VCDs are bias-corrected (Section 4.1).

6. Emissions Inversion Results

6.1. Observational Space Diagnostics

To assess whether the DA framework functions properly, we first examine the prior and posterior distributions of the model NO_2 and HCHO column innovations (i.e., observation

https://doi.org/10.5194/egusphere-2026-6714
Preprint. Discussion started: 17 November 2026
© Author(s) 2026. CC BY 4.0 License.

minus forecast) along with their associated statistical metrics, including mean bias (MB), root-mean-square error (RMSE), and correlation coefficient (R). A successful DA reduces the discrepancy between observations and model forecasts, as shown in Figure 4. The CTRL (a priori) simulation tends to overpredict TEMPO but underpredict TROPOMI NO_2 SCDs, as evidenced by the negative and positive innovations, respectively. The DA and emissions inversion effectively reduce errors in the prior forecast, lowering the RMSE from 3.5 to 2.03 $\times 10^{14}$ molec cm^{-2} in TEMPO-JOINT and from 3.65 to 2.7 $\times 10^{14}$ molec cm^{-2} in TROPOMI-JOINT, while increasing R in both experiments. For model HCHO columns, the CTRL simulation overestimates column abundances relative to both TEMPO and TROPOMI observations, with the innovation distributions skewed toward negative values. The posterior simulations from the emission inversion experiments successfully mitigate these positive biases, shifting the posterior innovation distributions so they are roughly centered on zero, with all statistical metrics showing marked improvements. Notably, the posterior model fields for both NO_2 and HCHO generally exhibit a closer fit to TEMPO observations than to TROPOMI.

We also evaluate the χ^2 statistic, defined as the ratio of the prior RMSE to the total ensemble spread (Ménard & Chang, 2000), which indicates whether the DA process is under- or over-fitting the observations. The diagnostic values for both NO_2 and HCHO columns at each DA cycle generally fluctuate between 0.7 and 1.3 across our emission inversion experiments. This demonstrates that our DA system is properly configured and operating optimally.

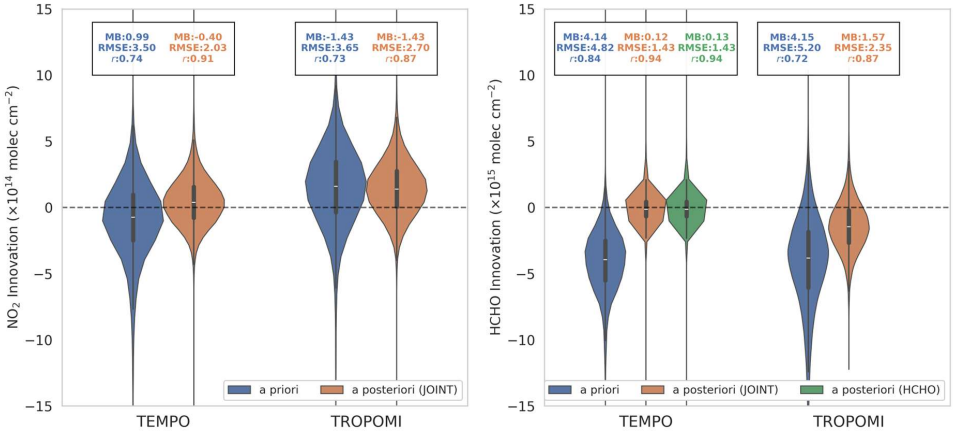


Figure 4. Distributions of prior and posterior WRF-Chem NO_2 (left) and HCHO (right) column innovations. Statistical metrics, including mean bias (MB), root-mean-square error (RMSE),

https://doi.org/10.5194/egusphere-2026-6714
Preprint. Discussion started: 17 November 2026
© Author(s) 2026. CC BY 4.0 License.

and the correlation coefficient (r), are displayed within the respective panels. Note that the MB is calculated as model minus observation, which is opposite in sign to the innovation.

6.2 Posterior NO_x Emissions Analysis

Figure 5 shows the spatiotemporal patterns of our top-down NO_x emissions. High NO_x emissions are primarily located in urban areas and along major highway systems across the CONUS, as displayed in the prior emission map (Figure 5a). Top-down NO_x emissions derived from the assimilation of TEMPO and TROPOMI NO_2 observations demonstrate large-scale similarities in the spatial patterns of adjustments, with emission reductions occurring across much of the central and northeastern US, and increases in the southeastern US and the Intermountain West (Figures 5b and 5c). More pronounced corrections are found in urban centers, where top-down NO_x emissions are generally lower by 10–40% across most cities with some exceptions such as Los Angeles (LA) and Raleigh, North Carolina where top-down NO_x emissions increased. Despite the overall resemblance between the satellite-derived NO_x emission estimates, prominent regional discrepancies exist (Figure 5d). For instance, TEMPO-JOINT yields higher posterior NO_x emissions in many major metropolitan areas (e.g., LA, Dallas, Atlanta, and NYC) and across the Midwest compared to the TROPOMI posterior NO_x emissions. Conversely, TROPOMI-derived emissions tend to be higher in rural and remote regions, the northwestern US, and the coastal region from Texas to Florida. This spatial discrepancy is consistent with the satellite NO_2 column differences previously highlighted in Figure 1c.

Figures 5e and 5f show the time series of daily average top-down NO_x emissions in urban areas and across the CONUS, respectively. Three distinct emission profiles—weekday, Saturday, and Sunday—are applied to the prior inventory, with weekdays having higher NO_x emissions than weekends. The daily variations in TEMPO- and TROPOMI-derived NO_x emissions are well-aligned, with average top-down urban emissions reduced by 5–30% over the simulation period. The magnitude of this emission adjustment varies over time; its scale increases during the first two weeks, causing top-down NO_x emissions to reach a minimum on August 20 (approximately 25% lower than the prior value) before rebounding slightly (Figure 5e). The average top-down NO_x emissions over the entire CONUS display a temporal pattern similar to that of the urban regions (Figure 5f). Notably, the TROPOMI-derived CONUS emissions show higher values in late August compared to the TEMPO-derived estimates. This is driven by a greater enhancement in TROPOMI NO_2 SCDs across the central and southern

https://doi.org/10.5194/egusphere-2026-6714
Preprint. Discussion started: 17 November 2026
© Author(s) 2026. CC BY 4.0 License.

US during this period, as previously reported by Hsu et al. (2026). The total ensemble mean top-down NO_x emissions during August 07-26 over the CONUS from the TEMPO-JOINT and TROPOMI-JOINT experiments are 189.7 and 186.4 gigagrams (Gg) (Table 3), which are 13.8% and 15.3% lower than the a priori estimates, respectively.

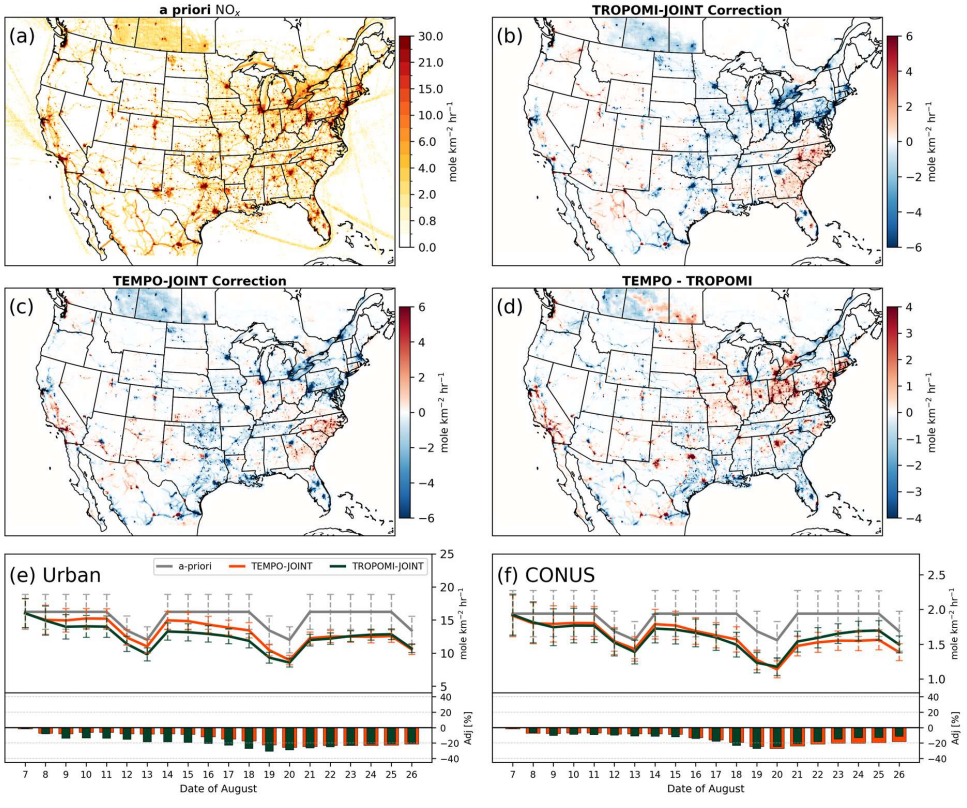


Figure 5. (a) Average a priori NO_x emissions, (b) average TROPOMI-JOINT a posteriori minus a priori NO_x, (c) average TEMPO-JOINT a posteriori minus a priori NO_x, (d) TEMPO-JOINT posterior minus TROPOMI-JOINT posterior NO_x emissions, (e) daily prior and posterior NO_x emissions and the relative emission adjustments for urban areas, and (f) daily prior and posterior NO_x emissions and the relative emission adjustments for the CONUS. The error bar in time series denotes ±1.96 ensemble spread around the ensemble mean emissions. The averaged emissions values are calculated based on data at 18 and 21 UTC.

6.3 Posterior NMVOC Emissions Analysis

6.3.1 Top-down Biogenic Emissions

https://doi.org/10.5194/egusphere-2026-6714
Preprint. Discussion started: 17 November 2026
© Author(s) 2026. CC BY 4.0 License.

This section examines the top-down biogenic isoprene emissions, as they account for a large fraction of total biogenic NMVOC emissions. Investigation of the top-down adjustment patterns of isoprene is crucial for evaluating our inversion results. Figure 6 shows the spatiotemporal patterns of the prior and posterior biogenic isoprene emissions. Over the CONUS, the CTRL (a priori) predicts elevated isoprene emissions in the southeastern US, the mountain ranges of western Mexico, and California (Figure 6a). This spatial distribution reflects the major biogenic emission hotspots in our model domain. The total prior biogenic isoprene emissions in the CTRL amount to 2.35 Teragram (Tg) over the CONUS and 1.00 Tg over the southeastern US during the simulation period. It is noted that we have reduced the reference biogenic isoprene emissions by 25% before the simulation.

Assimilating TEMPO and TROPOMI HCHO columns systematically lowers the biogenic isoprene emission estimates, as demonstrated in Figures 6b–6d. The TROPOMI-JOINT experiment yields the lowest top-down biogenic isoprene estimate. The emissions over the southeastern US are reduced to 0.46 Tg, representing a 54% decrease compared to the prior value (Figure 6b). The TEMPO-derived biogenic isoprene emissions show similar adjustment between the TEMPO-JOINT and TEMPO-HCHO runs (Figures 6c and 6d). These top-down estimates range from 1.31 to 1.33 Tg over CONUS and 0.64 to 0.65 Tg over the southeastern US, reflecting a more moderate reduction of approximately 35% relative to the prior value. Differences in top-down isoprene emissions between TEMPO-JOINT and TEMPO-HCHO primarily appear in the southeastern US, where slightly higher biogenic isoprene emissions (+10–15%) occur in the joint inversion across Texas, Louisiana, and Arkansas (Figure 6e).

Figure 6f displays the daily average prior and posterior biogenic isoprene emissions in the southeastern US. The prior emissions (gray curve) exhibit pronounced daily fluctuations driven by local meteorological conditions, reaching a minimum on August 16 and then gradually increasing. During the first half of the simulation (August 7–16), the top-down isoprene emissions show good agreement in both magnitude and temporal variation across all inversion experiments, with all estimates capturing the lowest isoprene emissions on August 16. However, the satellite-derived biogenic emission estimates diverge after August 16; the TEMPO-derived isoprene emissions increase over time, tracking the temporal pattern of the CTRL run, whereas the TROPOMI-derived values remain at low levels.

This substantially lower top-down estimate in the TROPOMI-JOINT run is attributed to the persistently low TROPOMI HCHO columns over the southern US during late August, a period during which TEMPO HCHO column abundances are increased (Figure S2). It is noted

https://doi.org/10.5194/egusphere-2026-6714
Preprint. Discussion started: 17 November 2026
© Author(s) 2026. CC BY 4.0 License.

that we already applied bias-correction to the TROPOMI HCHO data, which increased the HCHO columns by ~20%. The TROPOMI-derived isoprene emissions would be even lower without these adjustments. These discrepancies suggest that TROPOMI data biases may vary regionally and temporally, highlighting a need for further investigation. In summary, our emissions inversion suggests that the prior biogenic emissions are likely overestimated. The top-down estimates for other biogenic emission species behave similarly to isoprene, and these results are shown in Figure S3.

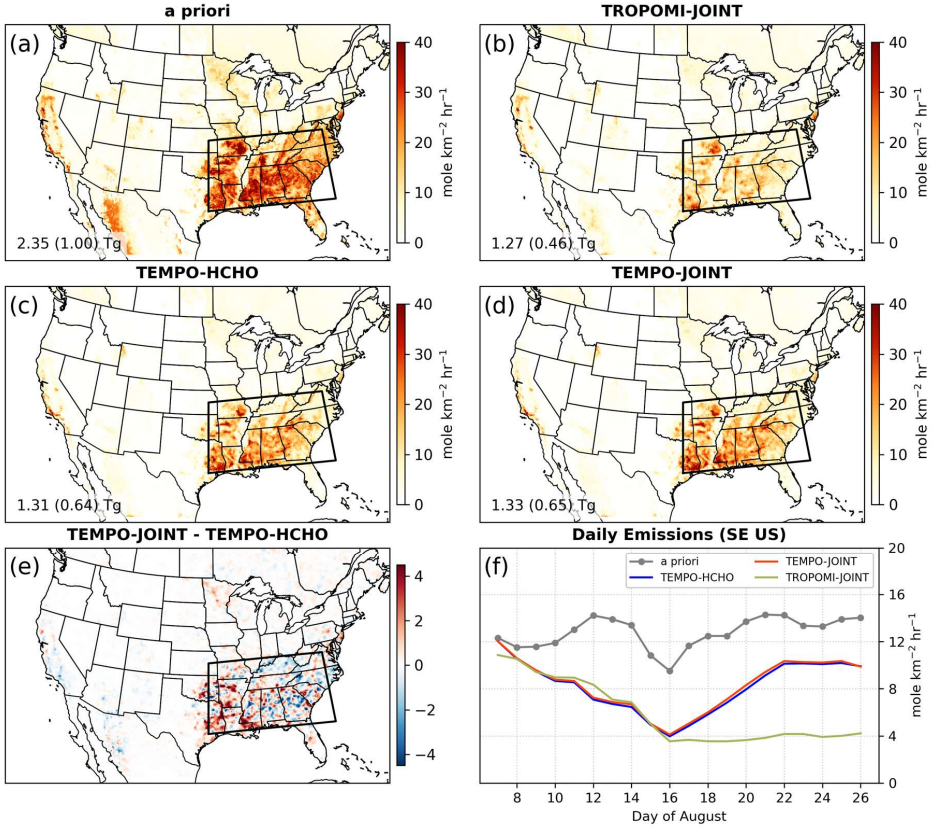


Figure 6. (a) Average biogenic isoprene emissions spatial distribution from CTRL, (b) Average biogenic isoprene emissions for TROPOMI-JOINT, (c) Average biogenic isoprene emissions for TEMPO-HCHO, (d) Average biogenic isoprene emissions for TEMPO-JOINT, (e) Difference between TEMPO-JOINT and the TEMPO-HCHO isoprene emissions, (f) Daily isoprene emissions time series over southeastern US. The values displayed on the lower left corner of panels a-d show the total isoprene emissions during the simulation time period of

https://doi.org/10.5194/egusphere-2026-6714
Preprint. Discussion started: 17 November 2026
© Author(s) 2026. CC BY 4.0 License.

August 07-26, 2023 for the CONUS and southeastern US (in parenthesis). The southeastern US is defined by the black box.

6.3.2 Top-down Anthropogenic NMVOC Emissions

To constrain the anthropogenic NMVOC (AVOC) emissions, we aggregate emissions into seven groups based on their chemical properties: alkanes, alkenes, aldehydes, alcohols, ketones, aromatics, and other VOCs (Table S2). Figure 7 illustrates the spatiotemporal variations of the prior and posterior total AVOC emissions. Prior AVOC emission hotspots primarily appear in urban areas, agricultural zones (e.g., California's Central Valley), and major oil and gas production regions, such as the Permian, Bakken, and Eagle Ford Basins (Figure 7a). The top-down total AVOC emissions across all inversion experiments exhibit a similar adjustment pattern, with posterior emissions predominantly reduced throughout most regions (Figures 7b–7d). Specifically, posterior total AVOC emissions are lowered by 10–40% relative to the prior estimates in urban cores and the Bakken and Eagle Ford production areas, indicating that prior AVOC emissions in these regions are likely overestimated. Notably, the TEMPO-derived AVOC adjustments exhibit an opposite direction over the Permian Basin, where top-down emissions are decreased in the northern portion but increased in the southern portion (Figures 7c and 7d).

The differences between the TEMPO-JOINT and TROPOMI-JOINT posterior total AVOC emissions are displayed in Figure 7e. Despite broad agreement in the large-scale emission adjustments, significant regional discrepancies remain. TEMPO-JOINT yields higher top-down AVOC emissions in many regions such as California, Oklahoma, North Carolina, and the Permian Basin, whereas TROPOMI-JOINT estimates higher emissions over the southeastern US and the Four Corners region. Furthermore, top-down AVOC emissions from TEMPO-JOINT are systematically higher than those from TEMPO-HCHO across the majority of the CONUS (Figure 7f). This difference is primarily driven by chemical feedbacks within the joint NO_x and NMVOC emission inversion framework, which are discussed in detail in Section 8.

Figures 7g and 7h display the time series of daily average prior and posterior total AVOC emissions over urban areas and the entire CONUS, respectively. The prior emissions (gray curve) exhibit minor variations between weekdays and weekends. Top-down AVOC emissions across all inversion experiments display highly consistent temporal patterns in urban areas, with posterior estimates continuously decreasing from August 7 to 16 before stabilizing in late

https://doi.org/10.5194/egusphere-2026-6714
Preprint. Discussion started: 17 November 2026
© Author(s) 2026. CC BY 4.0 License.

August (Figure 7g). The magnitudes of the average top-down AVOC emissions in TEMPO-JOINT and TROPOMI-JOINT are comparable, with both 30% lower than the prior estimates at the end of the simulation period. Additionally, the TEMPO-HCHO inversion exhibits the lowest top-down AVOC emissions among all experiments, running 10–15% lower than the TEMPO-JOINT simulation. The average top-down AVOC emissions on a CONUS scale closely resemble the temporal patterns observed in urban areas. However, the more pronounced daily fluctuations in the TEMPO-derived CONUS emissions are modulated by variability within the oil and gas production basins. Overall, top-down AVOC emissions are 10–20% lower than the prior value across all inversion experiments, with the TEMPO-JOINT run providing the highest top-down estimates on the CONUS scale.

The emission adjustments for individual AVOC groups are summarized in Table 3. Among all AVOC categories and inversion experiments, alkane emissions show the smallest changes, reflecting the relatively minor contribution of alkane oxidation to HCHO production compared to other NMVOC species in the US (Skipper et al., 2024). Emission adjustments for other AVOC categories display comparable magnitudes, with differences remaining within 3%. Alkene and aldehyde emissions generally exhibit the highest sensitivity and largest corrections when constrained by satellite HCHO columns, as these two precursor groups account for a large fraction of total HCHO production (Skipper et al., 2024).

Notably, top-down AVOC emissions in the joint inversion experiments (TEMPO-JOINT and TROPOMI-JOINT) are 4% to 9% higher than those from the experiment solely constraining AVOC emissions (TEMPO-HCHO) across various AVOC categories (Table 3). This difference is primarily driven by the impact of NO_x on HCHO production, which is discussed in detail in Section 8. The substantially higher top-down alkane emissions in TEMPO-JOINT are mainly associated with the oil and gas production sector, such as in the Permian Basin (Figure 7f), where HCHO production is highly sensitive to ambient NO_x concentrations (Dix et al., 2023). Total ensemble mean top-down AVOC emissions over the CONUS during August 7–26 amount to 913.5, 997.5, and 934.8 Gg for TEMPO-HCHO, TEMPO-JOINT, and TROPOMI-JOINT, respectively, representing reductions of 16.4%, 8.8%, and 11.3% relative to the a priori estimates.

https://doi.org/10.5194/egusphere-2026-6714
Preprint. Discussion started: 17 November 2026
© Author(s) 2026. CC BY 4.0 License.

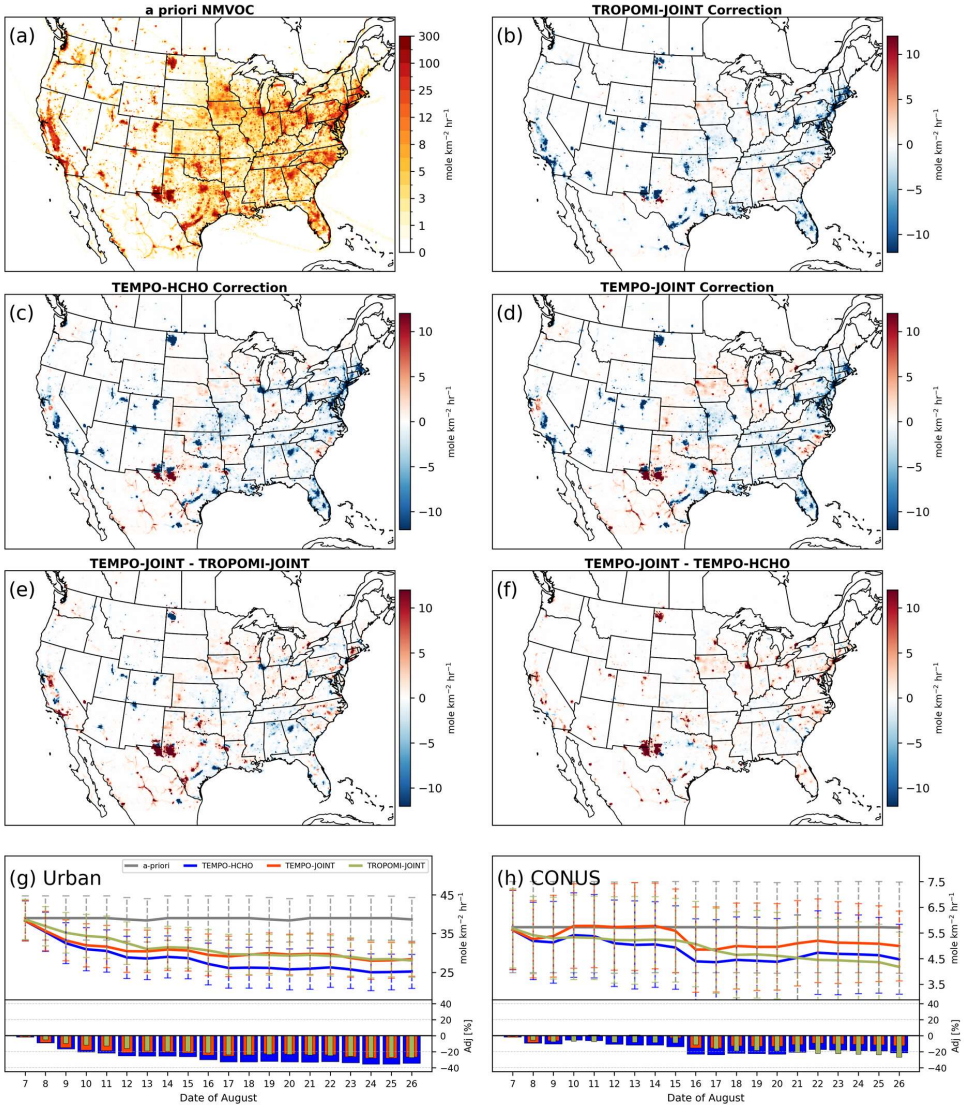


Figure 7. (a) Average a priori AVOC emissions spatial map, (b) difference between TROPOMI-JOINT and a priori AVOC emissions, (c) difference between TEMPO-HCHO and a priori AVOC emissions, (d) difference between TEMPO-JOINT and a priori AVOC emissions, (e) difference between TEMPO-JOINT and TROPOMI-JOINT AVOC emissions, (f) difference between TEMPO-JOINT and TEMPO-HCHO AVOC emissions, (g) daily prior and posterior total AVOC emissions and the relative emission adjustments for urban areas, and (h) daily prior and posterior total AVOC emissions and the relative emission adjustments for the CONUS. The error bar in time series denotes ±1.96 ensemble spread around the ensemble

https://doi.org/10.5194/egusphere-2026-6714
Preprint. Discussion started: 17 November 2026
© Author(s) 2026. CC BY 4.0 License.

mean emissions.

Table 3. Prior and posterior total NO_x and NMVOC emissions (Gigagram) over CONUS during the simulation time period. Values in parentheses are the percent change compared to the a priori.

	a priori	TEMPO-HCHO	TEMPO-JOINT	TROPOMI-JOINT
NO_x	220.2	N/A	189.7 (-13.8%)	186.4 (-15.3%)
Alkanes	628.7	538.1 (-14.4%)	595.9 (-5.2%)	537.9 (-14.4%)
Alkenes	48.8	39.9 (-18.2%)	42.7 (-12.6%)	41.6 (-14.7%)
Aldehydes	202.6	161.7 (-20.2%)	171.4 (-15.4%)	172.0 (-15.1%)
Alcohols	73.1	58.6 (-19.8%)	62.2 (-14.9%)	62.5 (-14.5%)
Ketones	59.8	49.3 (-17.6%)	52.4 (-12.4%)	51.7 (-13.5%)
Aromatic	33.2	27.2 (-18.0%)	29.1 (-12.2%)	28.3 (-14.7%)
Other	47.3	38.8 (-17.9%)	41.0 (-13.2%)	40.8 (-13.7%)
Isoprene (biogenic)	1822.8	1017.7 (-44.2%)	1035.7 (-43.2%)	911.0 (-50.0%)

7. Evaluation of Posterior Concentrations

7.1. Evaluation with CrIS Isoprene

We use CrIS isoprene data to evaluate the accuracy of our top-down biogenic isoprene emissions. The P_{90} value—defined as the atmospheric pressure below which 90% of the isoprene column resides—in the CrIS isoprene product is used to account for the vertical sensitivity of satellite observations (Wells et al., 2025). When comparing the model and CrIS isoprene data, the model P_{90} value is first calculated based on the vertical isoprene profile from the WRF-Chem simulation. The CrIS retrieval provides isoprene columns corresponding to a suite of P_{90} values at a given grid cell. The reported CrIS isoprene column is then interpolated to the P_{90} pressure value derived from WRF-Chem and compared with the WRF-Chem isoprene columns.

Figure 8 shows the time averaged maps of CrIS and model isoprene column concentrations during our simulation period. The isoprene column hotspots are mainly located in the southeastern US and the mountain ranges in northern California and western Colorado/Mexico. The CTRL run (a priori) nicely reproduces the spatial pattern of isoprene. However, the CTRL run shows markedly positive biases in isoprene abundance over these hotspot areas; for instance, the isoprene column is overestimated by 54% over the southeastern US. This indicates that the prior biogenic emissions could be substantially overestimated. In contrast, assimilation of TEMPO HCHO alone (TEMPO-HCHO) dramatically reduces this bias, to -17.2%. Further improvements are made through joint assimilation of TEMPO HCHO

https://doi.org/10.5194/egusphere-2026-6714
Preprint. Discussion started: 17 November 2026
© Author(s) 2026. CC BY 4.0 License.

and NO_2 (NMB = -11.3%), again demonstrating the value of multi-species assimilation. Despite this improvement, the posterior simulated isoprene columns in the southeastern US show a moderate underestimation. Model isoprene columns in other mountain regions (e.g., Mexico and California) also show underestimations, indicating that the biogenic isoprene emissions might be overcorrected after assimilating TEMPO HCHO data, potentially owing to biases in TEMPO HCHO data (Figure 3).

Assimilating TROPOMI HCHO also successfully mitigates the positive biases in the model isoprene columns. However, the TROPOMI-derived biogenic isoprene emissions are substantially underestimated, as the model isoprene shows a -41% bias compared to the CrIS data over the southeastern US. This indicates that the top-down biogenic emissions in TROPOMI-JOINT could be biased low and suffer from larger errors. It is also noted that the lower detection limit of CrIS isoprene is 2×10^{15} molec cm^{-2}, and observation values below this threshold should be interpreted with caution.

Our analysis suggests that the TEMPO HCHO data, as well as the joint inversion framework, provides a better constraint on biogenic isoprene emissions, especially over the southeastern US region.

https://doi.org/10.5194/egusphere-2026-6714
Preprint. Discussion started: 17 November 2026
© Author(s) 2026. CC BY 4.0 License.

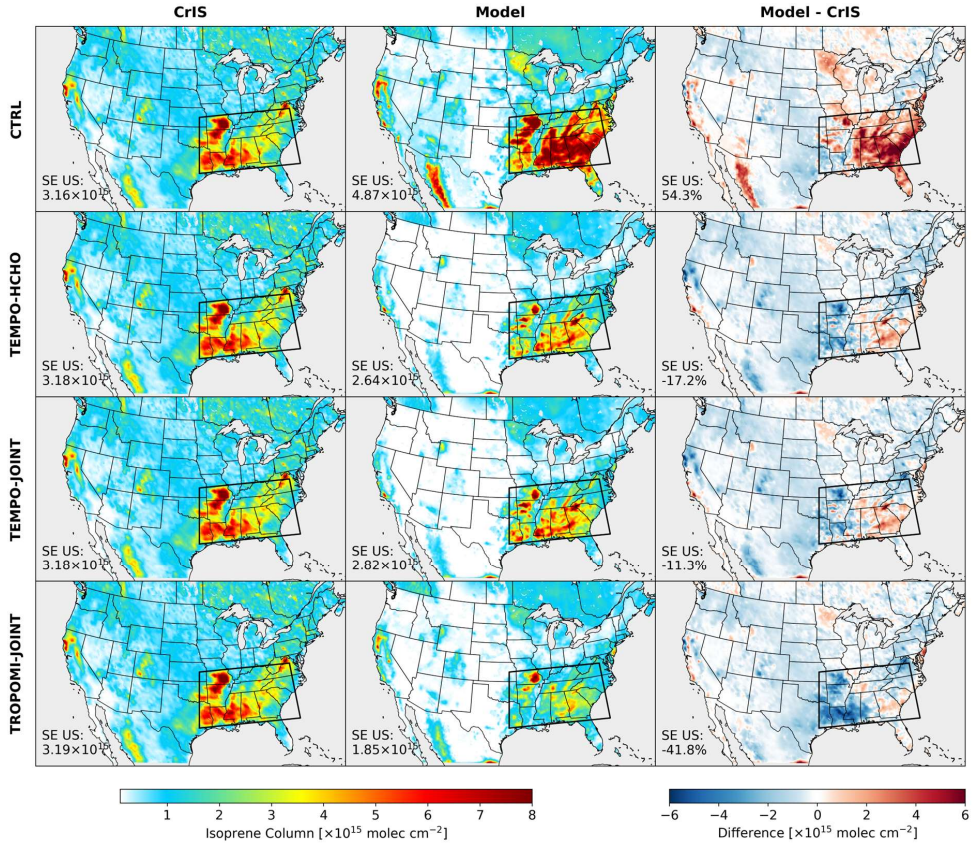


Figure 8. Averaged CrIS and model-simulated isoprene column concentrations during August 07-26. Each row from top to bottom shows the results from the CTRL, TEMPO-HCHO, TEMPO-JOINT, and TROPOMI-JOINT experiments, respectively. Each column from left to right displays the CrIS data (with P_{90} value adjustments based on the WRF-Chem isoprene profile), model-simulated isoprene columns, and the difference between the model and CrIS data. The black box denotes the southeastern US region. The average isoprene column abundances or the NMB are also listed in the lower-right corner of each panel.

7.2. Evaluation Against Surface HCHO Measurement

To assess the daily variation and the performance of the top-down NMVOC emissions, the daily average surface HCHO mixing ratios from the model ensemble mean and the observations are shown in Figure 9.

The CTRL run captures the daily fluctuations of the observed HCHO values, reproducing the low HCHO levels on August 15–16, followed by increases in late August at the South

https://doi.org/10.5194/egusphere-2026-6714
Preprint. Discussion started: 17 November 2026
© Author(s) 2026. CC BY 4.0 License.

DeKalb site (Atlanta) where elevated biogenic NMVOC emissions are present. However, CTRL considerably overpredicts the surface HCHO mixing ratio by +4.69 ppbv, consistent with the CrIS and model isoprene column comparison (Figure 8). The model-simulated HCHO mixing ratios from the top-down NMVOC emissions are greatly improved compared to the CTRL experiment, with the MB reduced to 1.80, 1.66, and 0.69 ppbv for the TEMPO-HCHO, TEMPO-JOINT, and TROPOMI-JOINT runs, respectively. The RMSEs are also lowered by 45–55% compared to the prior simulation. The posterior simulation using TEMPO-derived NMVOC emissions can better track the daily variation of surface HCHO at South DeKalb, and the level of HCHO agrees well with the observations. In contrast, the model HCHO mixing ratio from the TROPOMI-JOINT run shows a consistent underestimation after August 17. This is mainly attributed to the much lower top-down biogenic NMVOC emissions over the southeastern US, as discussed in Section 6.3.1. The evaluation against surface HCHO confirms that TROPOMI-derived biogenic emissions are biased low over the southeastern US even after applying bias correction and that TEMPO HCHO data can provide better top-down estimates in this region.

For the New Brunswick, Flax Pond, and Westport sites, the observed HCHO mixing ratios show similar magnitudes (1–3 ppbv) and temporal variations since these sites are located in the same vicinity. The observations show peak HCHO values on August 21 at all three sites, and the CTRL run is able to capture the temporal fluctuations of the HCHO mixing ratio well. Again, the CTRL run overestimates the HCHO mixing ratio by 0.86–2.39 ppbv, and all emissions inversion experiments successfully mitigate the positive biases and lower the errors to 0.24–1.39 ppbv across these sites. In this region, all inversion experiments demonstrate comparable results for simulating HCHO levels and daily variations, while TEMPO-JOINT and TEMPO-HCHO exhibit slightly better performance than TROPOMI-JOINT.

https://doi.org/10.5194/egusphere-2026-6714
Preprint. Discussion started: 17 November 2026
© Author(s) 2026. CC BY 4.0 License.

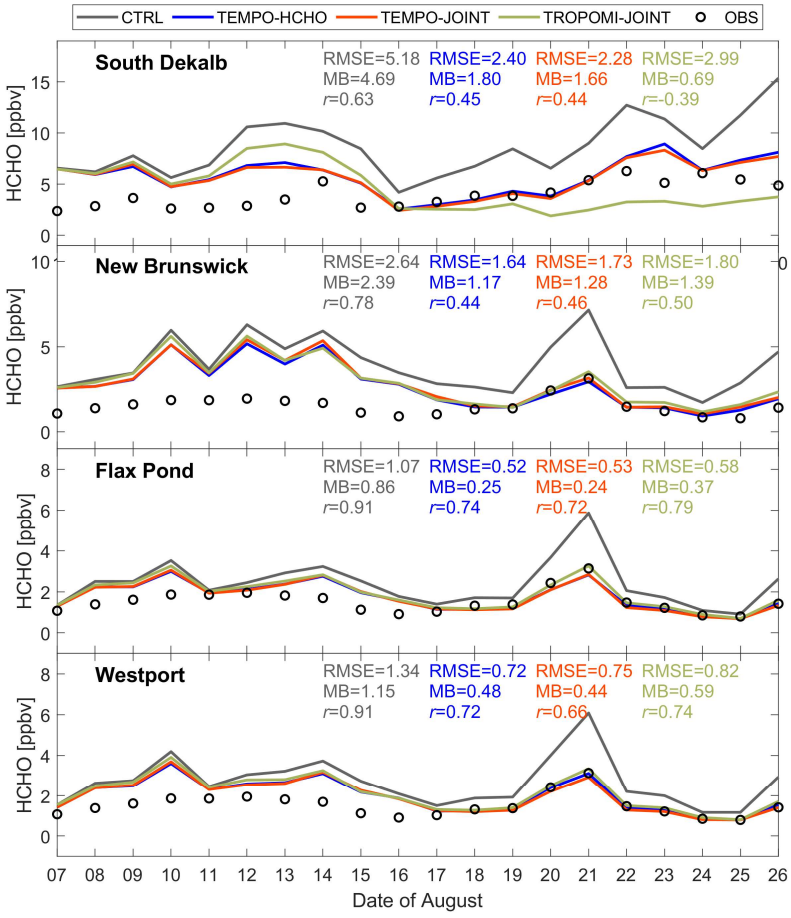


Figure 9. Daily average surface HCHO mixing ratios from observations and model ensemble mean from individual experiments. The statistics of RMSE, MB and *r* are also listed.

7.3 Evaluation Against AQS NO_2 and O_3 Observations

7.3.1. AQS NO_2 comparison

We evaluate the NO_x emissions inversion by comparing the ensemble mean of the WRF-Chem simulated surface NO_2 mixing ratios to the AQS observations. We applied a correction to the NO_2 observations made by molybdenum converter instruments following Lamsal et al. (2008) and Hsu et al. (2026) to account for the interference from other nitrogen compounds. This correction lowers the NO_2 measurements at affected sites by 10–20%.

Figure 10 shows the average surface NO_2 mixing ratio boxplots and time series from the emissions inversion experiments and observations. The CTRL (a priori) run underpredicts NO_2

https://doi.org/10.5194/egusphere-2026-6714
Preprint. Discussion started: 17 November 2026
© Author(s) 2026. CC BY 4.0 License.

mixing ratios as shown in the boxplot in Figure 10a, with NMB of -15.8% and RMSE of 3.09 ppbv. This underestimation is mainly because the model fails to capture high NO_2 values, as the boxplot distribution is skewed toward the lower end. Assimilating TEMPO and TROPOMI NO_2 SCDs leads to lower top-down NO_x emissions, as presented in Section 6.2. Therefore, the model-simulated NO_2 mixing ratios in TEMPO-JOINT and TROPOMI-JOINT are lower than CTRL, which further degrades the performance when compared to the observations, with the NMB degrading to -23.9% and -28.7%, respectively (Figure 10a). Since TEMPO-HCHO does not optimize NO_x emissions, the small difference between TEMPO-HCHO and CTRL NO_2 is due to the nonlinear chemical feedback within NMVOC-NO_x-OH interactions (Wolfe et al., 2016). In general, the impact of updating NMVOC emissions on NO_x concentrations is marginal (~1% in high-NO_2 environments) and can be disregarded during our simulation time period.

We further break down the AQS NO_2 data into urban, suburban, and rural sites to examine the top-down NO_x emissions in different environments, as shown in Figure 10b. The urban and suburban areas show elevated NO_2 mixing ratios ranging from 4–9 ppbv, while the values at rural sites are typically below 3 ppbv. The CTRL run struggles to simulate the high NO_2 mixing ratios in urban and suburban areas, where the model values are systematically biased low by 20.9% and 15.9%, respectively. In contrast, CTRL can nicely reproduce the NO_2 levels and temporal variability in the rural regions. The TEMPO-JOINT and TROPOMI-JOINT runs further exacerbate the underestimation of NO_2 in the urban and suburban regions, as the NMB degrades to -30% and -35.8%, while the rural regions are less impacted by the NO_x emissions inversion. This suggests that the top-down NO_x emissions in the urban areas are potentially biased low, especially for the TROPOMI-derived NO_x emissions, where larger error statistics of NMB and RMSE are observed compared to the TEMPO-derived emissions.

In addition to the NO_x emissions, the model resolution could also contribute to the errors in simulating NO_2 mixing ratios. The 12 km horizontal resolution used in this study may be insufficient to capture the fine-scale and localized NO_2 hotspots measured by the in situ instruments in urban and suburban areas (Sekiya et al., 2021; Valin et al., 2011; Yu et el., 2023).

https://doi.org/10.5194/egusphere-2026-6714
Preprint. Discussion started: 17 November 2026
© Author(s) 2026. CC BY 4.0 License.

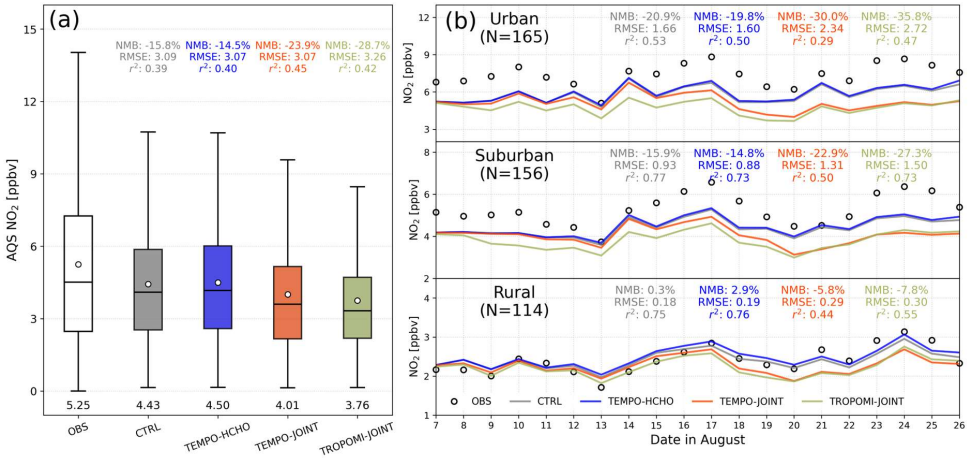


Figure 10. (a) Boxplots of average AQS and model-simulated NO_2 mixing ratios across individual sites. The circle symbols and the values listed at the bottom represent the mean fields, while the horizontal lines inside the boxes indicate the median values. The box represent data with 25-75 percentile and the whisker shows the data range of 5-95 percentile range. (b) Daily average AQS and model-simulated NO_2 time series in urban, suburban, and rural areas. The statistical metrics of NMB, RMSE, and the coefficient of determination (r^2) are also provided within the respective panels. The total monitoring sites (N) are also listed.

7.3.2 MDA8 O_3 comparison

We evaluate the model-simulated maximum daily 8-hour average (MDA8) O_3 to assess how the emissions inversion impacts the O_3 simulation. The average MDA8 O_3 values in urban, suburban, and rural regions are displayed in Figure 11.

The CTRL run captures the daily variation of MDA8 O_3 across different regions fairly well; however, MDA8 O_3 values are overpredicted by 4.4, 3.2, and 1.8 ppbv in urban, suburban, and rural areas, respectively. The CTRL forecast mean MDA8 O_3 across all sites has a tighter distribution and is skewed toward higher values compared to the shape from the AQS observations (Figure 11, right panel). The systematic overestimation of the observed MDA8 $O_3 < 35$ ppbv in the model can be attributed to the higher background O_3 values from the model boundary conditions, as the model forecasts a higher MDA8 O_3 along coastal regions as shown in Figure S4a.

Emissions inversion leads to improvements in forecasting MDA8 O_3, especially for urban and suburban areas as shown in Figures 11a–b. The TEMPO-HCHO experiment, which only optimizes NMVOC emissions, reduces the forecast mean MDA8 O_3 by 1.2, 1.0, and 0.8 ppbv

https://doi.org/10.5194/egusphere-2026-6714
Preprint. Discussion started: 17 November 2026
© Author(s) 2026. CC BY 4.0 License.

in urban, suburban, and rural areas, respectively (Figure 11, right panel). From a regional perspective, constraining NMVOC emissions alone helps to mitigate the O_3 overestimation from the central to northeastern US (Figures S4b–c) and reduces the positive biases by 2–6 ppbv. The O_3 production during our simulation period changes in the same direction as the NMVOC emissions adjustments in the CONUS. The largest impact appears in urban cores such as Los Angeles, Phoenix, Salt Lake City, and Chicago. This is because large urban areas are normally classified as transition or VOC-limited regimes in O_3 production (Jin et al., 2020; Simon et al., 2024; Stanier et al., 2021). A widespread impact can also be seen in the central US and Great Lakes regions (Figure S4f). In contrast, the southeastern and northwestern US show weak or opposite responses to the NMVOC emission changes, as these areas primarily reside in NO_x-limited regions (Jin et al., 2025).

The joint NO_x and NMVOC emissions inversion results in the lowest MDA8 O_3 forecast. This is owing to the reduction of top-down NO_x emissions, which further lowers O_3 production along with the NMVOC emissions adjustments. The NO_x emissions optimization contributes to a 1.9–2.2 ppbv mean MDA8 O_3 reduction when comparing the model output from TEMPO-JOINT and TEMPO-HCHO, with suburban and rural regions showing higher sensitivities to the NO_x emissions adjustments. The joint inversions (TEMPO-JOINT and TROPOMI-JOINT) exhibit the best performance in reproducing the magnitude and daily variation of MDA8 O_3 in urban areas, as the MB is reduced to 1.67 and 1.59 ppbv, respectively (Figure 11a). The peak and the distribution of mean MDA8 O_3 are also better aligned with the observations (Figure 11a, right panel). Nevertheless, the joint inversion leads to an underestimation of MDA8 O_3 in suburban and rural areas, particularly in late August (Figures 11b–c). Regionally, the joint emissions inversions effectively eliminates the MDA8 O_3 overprediction across the eastern US (Figures S4d–e) and show greater and more widespread impact on O_3 formation across the CONUS (Figure S4g) compared to NMVOC emissions optimization alone. This result also aligns with studies that the O3 production regime over the CONUS has been moving toward a more NO_x-limited regime (Jin et al., 2025; Zhu et al., 2022). The major difference between the two joint inversion experiments mainly appears over the southern US (Figure S4h), which is primarily driven by the lower NMVOC emissions in TROPOMI-JOINT (Figures 6 and 7e).

In summary, we demonstrate that the joint inversion performs the best in the MDA8 O_3 forecast compared to either constraining NO_x or NMVOC emissions alone, especially in urban areas. Despite the improvement, the O_3 production in our joint inversion experiments might be underestimated due to the potential low bias of our top-down NO_x emissions (Section 7.3.1).

https://doi.org/10.5194/egusphere-2026-6714
Preprint. Discussion started: 17 November 2026
© Author(s) 2026. CC BY 4.0 License.

This could explain why the joint inversion tends to underpredict MDA8 O_3 in suburban and rural areas, as the O_3 formation in these regions is more sensitive to NO_x emissions changes.

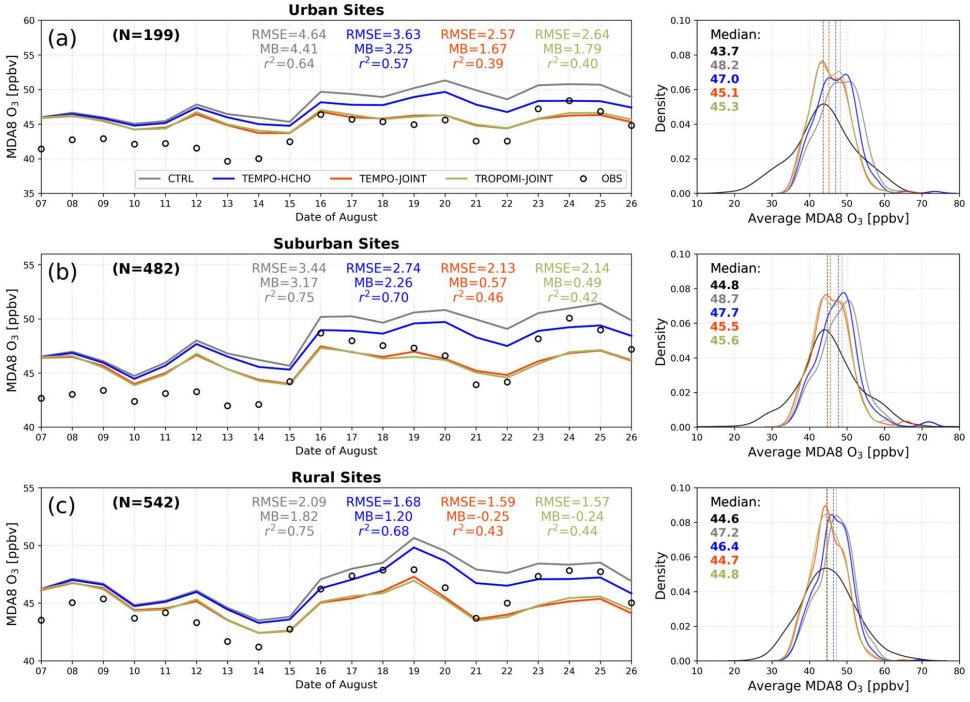


Figure 11. Time series and distributions of model-simulated and AQS MDA8 O_3 for (a) urban sites, (b) suburban sites, and (c) rural sites. The right panels display the distributions of the mean MDA8 O_3 values from individual observation sites within each category, and dashed line represents the median values. The statistical metrics of MB, RMSE, and r^2 are listed within the time series panels, and the median of the MDA8 O_3 values is provided within the right-hand distribution panels.

7.4 Evaluation Against DC-8 Aircraft Measurements

We evaluate the model-simulated trace gas mixing ratios by comparing them with the DC-8 aircraft measurements, as displayed in Figure 12. For this evaluation, we utilize DC-8 data collected over NYC on August 9 and 16, Chicago on August 8, 12, and 15, and LA on August 16, 23, and 25.

Figures 12a–d show the average model and observed DC-8 vertical profiles of NO_x, HCHO, isoprene, and O_3 below 3 km above ground level. The CTRL (a priori) run

https://doi.org/10.5194/egusphere-2026-6714
Preprint. Discussion started: 17 November 2026
© Author(s) 2026. CC BY 4.0 License.

underpredicts the NO_x mixing ratio by 15% and exhibits larger discrepancies near the surface. Conversely, the CTRL run markedly overpredicts HCHO and isoprene mixing ratios by 69% and 78%, respectively. These comparisons suggest a potential overestimation of prior NMVOC emissions and an underestimation of prior NO_x emissions in Chicago, NYC, and LA. For the O_3 simulation, the CTRL run shows a minor error with a NMB of -3.9%. While average near surface O_3 levels are well represented by the CTRL run, underestimation primarily occurs in regions above 500 meters.

Assimilating TEMPO and TROPOMI data improves the simulation of NO_x, HCHO, and isoprene. The TEMPO-JOINT and TROPOMI-JOINT runs increase average NO_x mixing ratios, particularly near the surface (Figure 12a). It is noted this NO_x behavior reflects opposing changes across the sampled cities as shown below. NMVOC emission inversions demonstrate substantial improvements in model HCHO and isoprene. The positive biases are greatly reduced by 40–70% across HCHO and isoprene, and the posterior vertical profiles show much better agreement with the DC-8 observations (Figures 12b–c). The HCHO and isoprene vertical profiles from TEMPO-JOINT and TEMPO-HCHO closely resemble each other, with differences of only 1% and 8%, respectively. Despite these improvements in NO_x and HCHO, the emission inversions slightly degrade O_3 simulation performance. The model-simulated O_3 mixing ratios are lower than those in the CTRL run, which increases the negative biases to 5–10% across all inversion experiments (Figure 12d).

The vertical profiles for individual flight dates are available in Figure S5. The CTRL run tends to overpredict NO_x in NYC and Chicago. Assimilating TEMPO and TROPOMI NO_2 ameliorates positive bias, however, the top-down emissions are over corrected which lead to underestimation of model NO_x profiles (Figure S5a). On the contrary, CTRL underpredicts NOx levels in LA and the top-down NOx emissions over LA are increased which improve the agreement between model and observations, especially when assimilating TEMPO NO_2 data. Noted that the vertical profiles from the TROPOMI-JOINT show large deviations from TEMPO-JOINT for HCHO, isoprene, and O_3, which is heavily driven by large errors over LA. TROPOMI-JOINT underestimates HCHO, especially near the surface, and also underestimates isoprene (-71% to 77%) compared to observations during late August (Figures S5a–b), whereas it remains comparable to TEMPO-JOINT over NYC and Chicago. This indicates that the TROPOMI-derived biogenic and anthropogenic NMVOC emissions in late August suffer from large errors in the LA basin. These low top-down NMVOC emissions in TROPOMI-JOINT subsequently result in low O_3 levels over LA (Figure S5d). Also, the TEMPO-derived biogenic

https://doi.org/10.5194/egusphere-2026-6714
Preprint. Discussion started: 17 November 2026
© Author(s) 2026. CC BY 4.0 License.

isoprene emissions are overestimated on August 25–26. The model-simulated isoprene mixing ratios are biased high, which contributes to the sharp increase in the near-surface average isoprene values seen in the profile in Figure 12c.

To further assess the performance of the NMVOC emissions inversion, we compare model VOC species that can be directly mapped to the aircraft observations, with the results shown in Figure 12e. We only use observations below 2 km (i.e., within the planetary boundary layer) for this evaluation. Without optimizing NMVOC emissions, the CTRL run substantially overpredicts the mixing ratios of most VOC species, with NMB values ranging from 9% to 200%, further suggesting that prior NMVOC emissions are overestimated across these three cities. The only two exceptions are ethane and monoterpenes, for which the model is biased low by 10% and 8.6%, respectively. Assimilating TEMPO HCHO columns effectively reduces the positive biases in the model-simulated VOCs. Aromatics (benzene, toluene), alkenes (ethene, isoprene), and alcohols show relatively large improvements, with positive biases reduced by 30–90%. However, due to the reduced top-down NMVOC emissions across all species, the posterior emissions exacerbate underestimations for VOC species that were already biased low in the CTRL run, such as ethane. The performances of TEMPO-HCHO and TEMPO-JOINT in constraining various VOC emissions and species are generally comparable, with differences for most species within 2%. Overall, the joint inversion framework performs slightly better in capturing isoprene and HCHO levels than updating solely NMVOC emissions in these three cities. In contrast, the TROPOMI-JOINT experiment greatly underpredicts most VOC species, primarily due to the severe model underestimation over the LA region. This indicates that both anthropogenic and biogenic NMVOC emissions are not well constrained over LA when using TROPOMI HCHO data during late August.

Our analysis demonstrates that the joint emission inversion framework shows a promising capability to update NO_x and NMVOC emissions over NYC, Chicago, and LA, and highlights that the TEMPO data provides a higher-quality constraint for inferring these emissions.

https://doi.org/10.5194/egusphere-2026-6714
Preprint. Discussion started: 17 November 2026
© Author(s) 2026. CC BY 4.0 License.

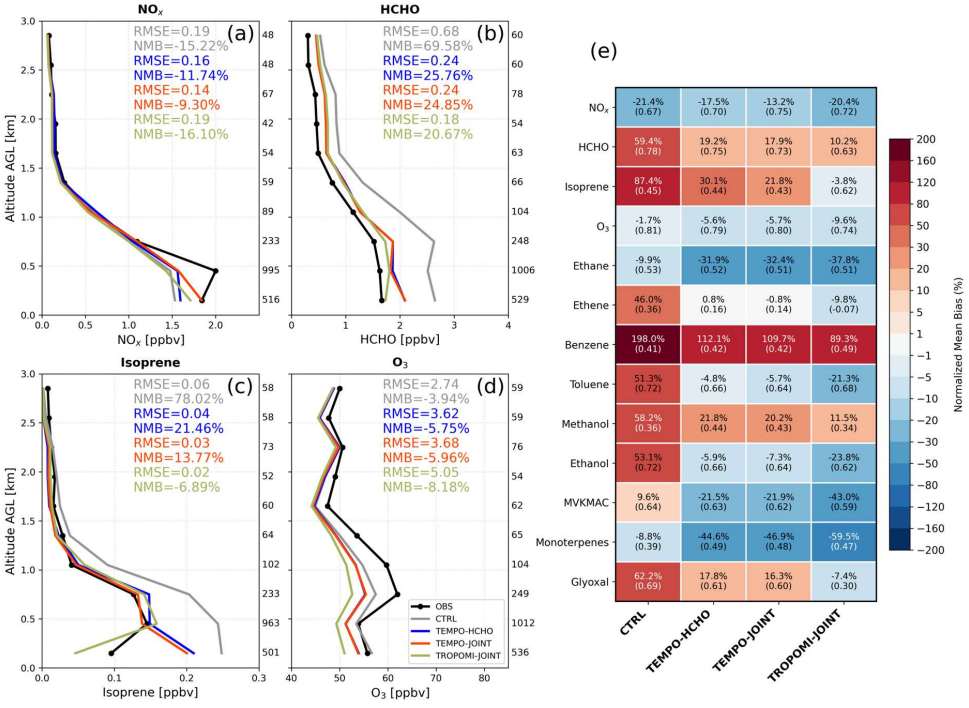


Figure 12. Average DC-8 observed and model ensemble mean vertical profiles of (a) NO_x, (b) HCHO, (c) isoprene, and (d) O_3 below 3 km above ground level. (e) The NMB (%) and correlation coefficient *r* (in parentheses) for various species. The statistical metrics (MB and RMSE) listed within the vertical profile panels (a–d) are calculated using data collected below 3 km above ground level. The value on the right vertical axis of vertical profiles represents the number of DC-8 observations. The NMB and *r* in panel (e) only consider data within 2 km AGL.

8. Impact of Joint Inversion on Top-Down NMVOC Emissions

In this section, we discuss how the joint inversion affects the NMVOC emissions quantification, given that the top-down NMVOC emissions in TEMPO-JOINT are about 10% higher than those from the TEMPO-HCHO run (Figure 7). We attribute this difference to the chemical feedback within the NO_x-OH-VOC atmospheric system. To elucidate this mechanism, we calculate the model total NO_2, HCHO, and OH columns at each grid point from the CTRL, TEMPO-HCHO, and TEMPO-JOINT experiments. The model columns between 18 and 21 UTC (midday hours) are averaged, and only land-based grid cells are used for this analysis.

Figure 13a shows the scatter plot of the HCHO and OH column differences between the

https://doi.org/10.5194/egusphere-2026-6714
Preprint. Discussion started: 17 November 2026
© Author(s) 2026. CC BY 4.0 License.

TEMPO-HCHO and CTRL runs. Because the top-down NMVOC emissions are lower than the prior estimates, ΔHCHO shows negative values while OH increases by 5-30%. They are inversely correlated (r = -0.75) because the chemical consumption of OH by NMVOCs is reduced in the TEMPO-HCHO experiment. Figure 13b shows HCHO versus NO_2 column differences between the TEMPO-HCHO and CTRL runs. No clear relationship is observed between the changes in HCHO columns and NO_2 columns, as the data points are highly scattered with a near-zero correlation (r = 0.07). This indicates that optimizing NMVOC emissions alone has no systematic, widespread impact on NO_x abundances in our model.

Figures 13c and 13d compare the column differences between TEMPO-JOINT and TEMPO-HCHO to assess how the NO_x emission adjustments impact the overall chemical system. When enabling the NO_x emissions inversion, ΔNO_2 is positively correlated (r = 0.67) with ΔOH, as illustrated in Figure 13c. Notably, the NO_2-OH relationship exhibits a strong linear correlation in relatively low-NO_2 environments, whereas a highly non-linear relationship emerges under high-NO_2 conditions. This non-linear behavior occurs because in high-NO_x environments like urban cores, the reaction of NO_2 and OH becomes the dominant sink for hydrogen oxide radicals (HO_x). In this regime, reducing NO_x emissions reduces the suppression of OH by weakening this termination pathway. This chemical feedback offsets the linear decrease in OH driven by the reduction of peroxy radical propagation ($HO_2 + NO \rightarrow OH + NO_2$ as well as $RO_2 + NO \rightarrow RO + NO_2$, which subsequently regenerates HO_2). Consequently, weakening this propagation slows the decrease in OH, causing ΔOH to flatten out or even turn slightly positive despite large drops in ΔNO_2.

The model-simulated HCHO columns also display a positive correlation (r = 0.57) with NO_2 levels, as demonstrated in Figure 13d, mirroring the NO_2-OH response. This positive relationship is driven by two reinforcing mechanisms. First, because HCHO is primarily produced via the oxidation of NMVOCs by OH, a decrease in NO_x emissions lowers OH abundances across most regions, extending VOC lifetimes and slowing HCHO formation. Second, lower NO_x also inherently decreases the HCHO yield from many VOCs, such as isoprene (Wolfe et al., 2016). Under this positive NO_x-OH-HCHO feedback mechanism, when the top-down NO_x emissions are lower than the prior estimates, the VOC lifetime in the TEMPO-JOINT run increases, resulting in a lower HCHO forecast. This lower HCHO forecast reduces the prior innovation (i.e., Observation minus Forecast) as our model simulation tends to overpredict HCHO columns. Consequently, the DA system applies a smaller downward correction to the NMVOC emissions.

https://doi.org/10.5194/egusphere-2026-6714
Preprint. Discussion started: 17 November 2026
© Author(s) 2026. CC BY 4.0 License.

This positive NO_x-OH-HCHO chemical feedback explains why the joint inversion (TEMPO-JOINT) ultimately leads to higher top-down NMVOC emissions than the NMVOC-only inversion (TEMPO-HCHO). This tightly coupled chemistry also highlights how observational errors can propagate across species within a joint DA framework. Satellite NO_2 retrievals may exhibit an underlying low bias, as indicated by evaluation against Pandora. If left uncorrected, this systematic error can inadvertently drive spurious adjustments in the satellite-derived NMVOC emissions. Therefore, while our results demonstrate the benefits of joint DA over single-species inversions, they equally show that rigorous satellite bias corrections are essential prior to assimilation. Mitigating retrieval biases is critical not only for accurately constraining NO_x emissions, but also for preventing systematic errors from cascading into top-down NMVOC emission estimates.

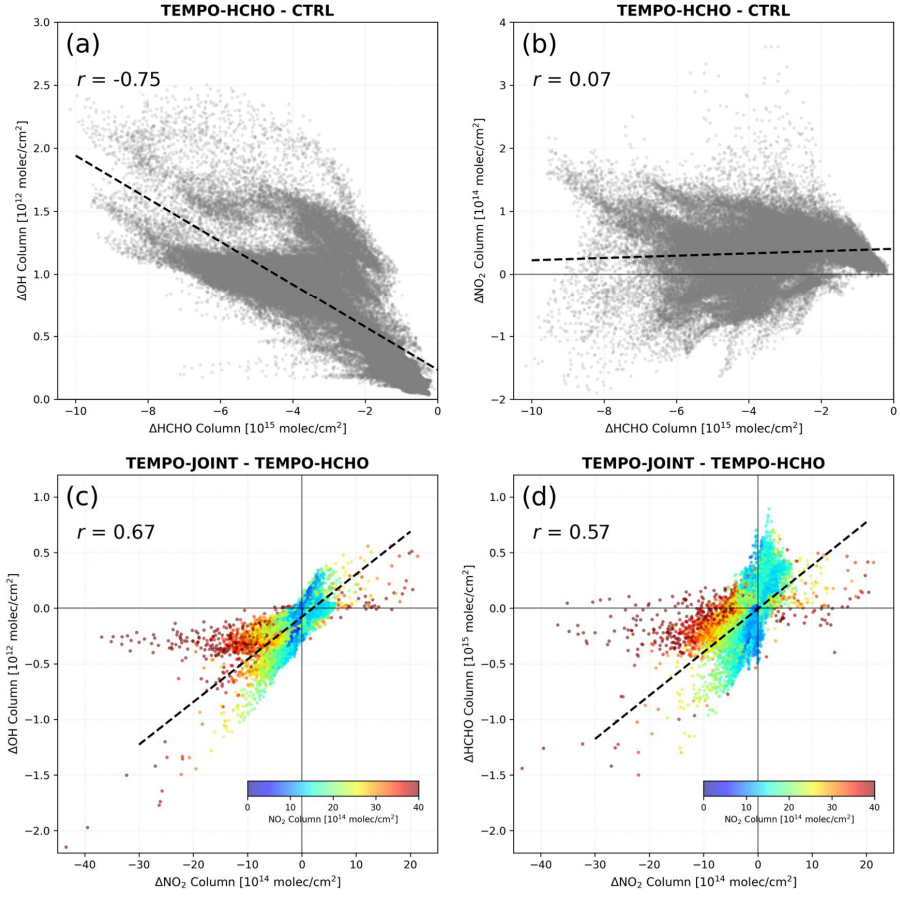


Figure 13. Scatter plots illustrating the domain-wide non-linear chemical feedback over land.

https://doi.org/10.5194/egusphere-2026-6714
Preprint. Discussion started: 17 November 2026
© Author(s) 2026. CC BY 4.0 License.

(a) HCHO and OH column differences between TEMPO-HCHO and CTRL, (b) HCHO and NO_2 column differences (TEMPO-HCHO minus CTRL), (c) OH and NO_2 column differences (TEMPO-JOINT minus TEMPO-HCHO), and (d) HCHO and NO_2 column differences (TEMPO-JOINT minus TEMPO-HCHO). The black dashed lines represent the regression line, and the corresponding correlation coefficients (*r*) are provided in each panel. In panels (c) and (d), the data points are color-coded by the NO_2 column abundance from the TEMPO-HCHO to differentiate between low- and high-NO_x chemical regimes.

9. Conclusion

In this study, we developed and evaluated a multi-species top-down emission inversion framework using the WRF-Chem/Chem-DART modeling system to simultaneously constrain anthropogenic and biogenic NO_x and NMVOC emissions, leveraging midday TEMPO (only 18 and 21 UTC) and TROPOMI remote sensing data. Prior to DA, evaluation against ground-based Pandora instruments revealed that both TEMPO and TROPOMI NO_2 and HCHO tropospheric VCDs were biased low, with larger inaccuracies observed in the TEMPO retrievals during early morning hours. Midday TEMPO data exhibited a bias pattern comparable to that of TROPOMI.

Top-down NO_x emissions inferred from both the TEMPO-JOINT and TROPOMI-JOINT runs were 5% to 30% lower than the a priori estimates across most regions during the simulation period, with the most pronounced reductions occurring in urban cores. This reduction in NO_x emissions exacerbated the model's underestimation of surface NO_2 mixing ratios when evaluated against the AQS data, indicating that the satellite-derived urban NO_x emissions may be biased low. Conversely, top-down NO_x emissions were adjusted upward in the LA Basin, bringing the posterior simulation into closer agreement with in situ aircraft measurements. Overall, the TEMPO-derived NO_x emissions were higher than the TROPOMI-derived values and yielded better error metrics when validated against independent observations.

Our emission inversion also suggested a widespread overestimation in the prior inventory for both anthropogenic and biogenic NMVOCs, with posterior anthropogenic and biogenic emissions showing a reduction of 20%-40% and 30%-70%, respectively, particularly when assimilating TROPOMI HCHO columns. Comprehensive evaluations against independent VOC measurements confirmed that the a priori emissions were substantially biased high. The emissions inversion effectively mitigated these positive discrepancies, reducing the systematic

https://doi.org/10.5194/egusphere-2026-6714
Preprint. Discussion started: 17 November 2026
© Author(s) 2026. CC BY 4.0 License.

biases of the model-simulated isoprene columns over the southeastern US and cutting the errors of most boundary-layer VOC species by 30% to 90% relative to the DC-8 aircraft profiles. However, the TROPOMI-JOINT run demonstrated large inaccuracies over the southern US in late August even after bias correction. This discrepancy strongly suggests that TEMPO's higher retrieval data quality and spatial consistency during midday hours provide a more robust and reliable constraint on regional NMVOC emissions than TROPOMI data during this timeframe.

On average, the joint inversion framework showed the best performance in forecasting MDA8 O_3 across urban areas, effectively eliminating the systematic overestimation of surface ozone in the prior simulation, although an underestimation of top-down NO_x emissions could lead to an excessive reduction in simulated O_3 production. We investigated how the top-down NMVOC emissions responded to the joint versus NMVOC-only inversion through the lens of non-linear chemical feedback. While single-species optimizations (TEMPO-HCHO) omit critical radical propagation pathways, the joint inversion (TEMPO-JOINT) actively modulates the atmospheric oxidizing capacity (i.e., local OH radical levels) by simultaneously adjusting NO_x emissions. This adjustment alters the atmospheric lifetimes of ambient VOCs and the NO-dependent secondary production rates of HCHO. This positive NO_x-OH-VOC chemical feedback loop explains why the joint framework derived 10% higher top-down NMVOC emissions than the NMVOC-only inversion, highlighting the need for integrated multi-species inverse modeling.

Despite these major advancements, several challenges remain for future satellite-based emission inversions. First, the systematic biases in satellite NO_2 and HCHO retrievals can propagate directly into top-down emission estimates; hence, proper bias-corrections should be incorporated into future inversion setups. Additionally, the complex spatiotemporal dependencies embedded within satellite biases—as demonstrated by the TROPOMI HCHO data—underscore the need for a more sophisticated, spatiotemporal-aware bias-correction method to fully exploit the potential of satellite observations. Second, our validation against DC-8 data revealed highly variable error characteristics across different VOC species, demonstrating that assimilating HCHO columns alone is insufficient to constrain individual NMVOC species due to varying HCHO production yields across different VOC groups. Future emissions inversion frameworks can explore assimilating multi-spaceborne VOC data, such as glyoxal (Cao et al., 2018), isoprene (Wells et al., 2020), and ethane (Brewer et al., 2024; Francoeur et al., 2025), or utilizing surface O_3 observations (Kong et al., 2024; Ma et al., 2019) in conjunction with HCHO data to provide additional constraints on NMVOC emissions (Choi

https://doi.org/10.5194/egusphere-2026-6714
Preprint. Discussion started: 17 November 2026
© Author(s) 2026. CC BY 4.0 License.

et al., 2025).

In conclusion, our study demonstrates that high-quality midday TEMPO observations enable improved top-down NO_x and NMVOC emissions over the CONUS compared to TROPOMI data, an improvement driven primarily by TEMPO's superior midday retrieval fidelity rather than the utilization of full diurnal sampling. While this work demonstrates the immediate value of TEMPO's improved data quality, expanding the assimilation framework to ingest multi-hour observations across the full day will be essential to fully harness the diurnal capabilities of GEO satellite platforms. With the ongoing refinement of satellite retrievals and the emergence of new spaceborne atmospheric composition products (Millet et al., 2024; Oomen et al., 2026), the inversion framework developed in this work establishes a solid foundation for high-resolution, multi-species top-down emission estimates, directly supporting air quality diagnostics, inventory evaluations, and the development of targeted emission mitigation strategies.

Data availability

The TEMPO/TROPOMI NO_2 and HCHO retrievals are obtained from NASA EARTHDATA (https://www.earthdata.nasa.gov/). The GRA^{2}PES emissions are available at: https://csl.noaa.gov/groups/csl4/gra2pes/. Surface HCHO observation at Atlanta is available at: https://github.com/KaiserLab-GeorgiaTech/long-term-HCHO-monitoring_efforts_datasets. Other surface HCHO observation can be obtained from: https://www-air.larc.nasa.gov/cgi-bin/ArcView/listos.2023.

Author contributions

CHH: Conceptualization, Formal analysis, Investigation, Methodology, Software, Visualization, Writing (original draft preparation). DKH, APM, BCM, ORC, RHS: Investigation, Supervision. DKH, BCM: Funding acquisition. CH, JH, ML, DBM, KCW, JK, SK, KHB, RBP, CBF, SW, GGA, CRN, XL, ZW, PR, CW, MMC, CES, JP, NBS, JZ, ADR, EMW, LX: Resources. All authors: Writing (review and editing).

Acknowledgements.

We acknowledge support from the NOAA High Performance Computing and the Alpine high performance computing resource at the University of Colorado Boulder. Alpine is jointly funded by the University of Colorado Boulder, the University of Colorado Anschutz, and

https://doi.org/10.5194/egusphere-2026-6714
Preprint. Discussion started: 17 November 2026
© Author(s) 2026. CC BY 4.0 License.

Colorado State University and with support from NSF Grants OAC-2201538 and OAC-2322260. Data storage is supported by the University of Colorado Boulder "PetaLibrary." The development of Chem-DART and Dr. Mizzi's participation is supported by NASA through the NASA Postdoctoral Program (NPP), Ames Research Center (ARC), Tropospheric Composition Program (TCP), and the NASA Earth Exchange (NEX). DART is supported by the National Science Foundation—National Center for Atmospheric Research (NSF-NCAR). We thank Dr. Caroline C. Womack and the ACES instrument team for providing the airborne glyoxal observations collected aboard the NASA DC-8 aircraft during the 2023 AEROMMA campaign. We thank Dr. Glenn M. Wolfe and the ISAF instrument team for providing the airborne formaldehyde observations collected aboard the NASA DC-8 aircraft during the 2023 AEROMMA campaign.

Financial support.

This research was supported by the NOAA GeoXO Program and NOAA cooperative agreement NA22OAR4320151, for the Cooperative Institute for Earth System Research and Data Science (CIESRDS). The TEMPO Mission is supported by NASA TEMPO Grant NNL13AA09C and NASA SNWG TEMPO Near Real Time Grant 80MSFC24CA004. HCHO measurements in Atlanta were supported by NASA Grant 80NSSC21K0944. DBM and KCW acknowledge support from NASA MEaSUREs (Grant 80NSSC24M0037).

Competing interests

At least one of the (co-)authors is a member of the editorial board of Atmospheric Chemistry and Physics.

References

Abdi-Oskouei, M., Barré, J., Wei, S., Lu, C., Griffin, A., Gas, C. H., et al. (2026). Capability Demonstration of a JEDI-Based System for TEMPO Assimilation: System Description and Evaluation. *Journal of Advances in Modeling Earth Systems*, *18*(5). https://doi.org/10.1029/2025ms005482

Achakulwisut, P., Brauer, M., Hystad, P., & Anenberg, S. C. (2019). Global, national, and urban burdens of paediatric asthma incidence attributable to ambient NO_2 pollution: estimates from global datasets. *The Lancet Planetary Health*, *3*(4), e166–e178. https://doi.org/10.1016/s2542-5196(19)30046-4

https://doi.org/10.5194/egusphere-2026-6714
Preprint. Discussion started: 17 November 2026
© Author(s) 2026. CC BY 4.0 License.

Anderson, J. L. (2001). An ensemble adjustment Kalman filter for data assimilation. *Monthly Weather Review*, *129*(12), 2884–2903. https://doi.org/10.1175/1520-0493(2001)129

Anderson, J. L. (2003). A local least squares framework for ensemble filtering. *Monthly Weather Review*, *131*(4), 634–642. https://doi.org/10.1175/1520-0493(2003)131

Anderson, J., Hoar, T., Raeder, K., Liu, H., Collins, N., Torn, R., & Avellano, A. (2009). The Data Assimilation Research Testbed: A Community Facility. *Bulletin of the American Meteorological Society*, 90(9), 1283–1296. https://doi.org/10.1175/2009bams2618.1

Bash, J. O., Baker, K. R., & Beaver, M. R. (2016). Evaluation of improved land use and canopy representation in BEIS v3.61 with biogenic VOC measurements in California. *Geoscientific Model Development*, *9*(6), 2191–2207. https://doi.org/10.5194/gmd-9-2191-2016

Bauwens, M., Stavrakou, T., Müller, J. F., De Smedt, I., Van Roozendael, M., van der Werf, G. R., et al. (2016). Nine years of global hydrocarbon emissions based on source inversion of OMI formaldehyde observations. *Atmospheric Chemistry and Physics*, *16*(15), 10133–10158. https://doi.org/10.5194/acp-16-10133-2016

Bourgeois, I., Peischl, J., Thompson, C. R., Aikin, K. C., Campos, T., Clark, H., Commane, R., Daube, B., Diskin, G. W., Elkins, J. W., Gao, R., Gaudel, A., Hintsa, E. J., Johnson, B. J., Kivi, R., McKain, K., Moore, F. L., Parrish, D. D., Querel, R., . . . Ryerson, T. B. (2020). Global-scale distribution of ozone in the remote troposphere from the ATom and HIPPO airborne field missions. *Atmospheric Chemistry and Physics*, *20*(17), 10611–10635. https://doi.org/10.5194/acp-20-10611-2020

Beaudry, S. J., & Cohen, R. C. (2026). A Signal-Derived retrieval reduces bias in TEMPO NO_2. *Journal of Geophysical Research Atmospheres*, *131*(8). https://doi.org/10.1029/2025jd045606

Brewer, J. F., Millet, D. B., Wells, K. C., Payne, V. H., Kulawik, S., Vigouroux, C., et al. (2024). Space-based observations of tropospheric ethane map emissions from fossil fuel extraction. *Nature Communications*, *15*(1), 7829. https://doi.org/10.1038/s41467-024-52247-z

Browne, E. C., Wooldridge, P. J., Min, K., & Cohen, R. C. (2014). On the role of monoterpene chemistry in the remote continental boundary layer. *Atmospheric Chemistry and Physics*, *14*(3), 1225–1238. https://doi.org/10.5194/acp-14-1225-2014

Cao, H., Fu, T. M., Zhang, L., Henze, D. K., Miller, C. C., Lerot, C., et al. (2018). Adjoint inversion of Chinese non-methane volatile organic compound emissions using space-

https://doi.org/10.5194/egusphere-2026-6714
Preprint. Discussion started: 17 November 2026
© Author(s) 2026. CC BY 4.0 License.

based observations of formaldehyde and glyoxal. *Atmospheric Chemistry and Physics*, *18(20)*, 15017–15046. https://doi.org/10.5194/acp-18-15017-2018

Cao, Y., Yue, X., Lei, Y., Zhou, H., Liao, H., Song, Y.,et al. (2021). Identifying the drivers of modeling uncertainties in isoprene emissions: schemes versus meteorological forcings. *Journal of Geophysical Research Atmospheres*, *126*(18). https://doi.org/10.1029/2020jd034242

Cazorla, M., Wolfe, G. M., Bailey, S. A., Swanson, A. K., Arkinson, H. L., & Hanisco, T. F. (2015). A new airborne laser-induced fluorescence instrument for in situ detection of formaldehyde throughout the troposphere and lower stratosphere. *Atmospheric Measurement Techniques*, *8*(2), 541–552. https://doi.org/10.5194/amt-8-541-2015

Chace, W. S., Womack, C., Ball, K., Bates, K. H., Bohn, B., Coggon, M., et al. (2025). Ozone Production Efficiencies in the Three Largest United States Cities from Airborne Measurements. *Environmental Science & Technology*, *59*(26), 13306–13318. https://doi.org/10.1021/acs.est.5c02073

Chi, N. D. T., Tanimoto, H., Inomata, S., Fujinawa, T., Müller, A., Sugita, T., et al. (2025). Characterization of Pandora Sky-Scan Modes from the Japan Pandora Network and Evaluation of Their Use in Validating Satellite NO_2 and HCHO Retrievals. *ACS ES&T Air*, *2*(12), 2872–2888. https://doi.org/10.1021/acsestair.5c00223

Choi, J., Henze, D. K., Cao, H., Nowlan, C. R., González Abad, G., Kwon, H., et al. (2022). An Inversion Framework for Optimizing Non-Methane VOC Emissions Using Remote Sensing and Airborne Observations in Northeast Asia During the KORUS-AQ Field Campaign. *Journal of Geophysical Research: Atmospheres*, *127(7)*. https://doi.org/10.1029/2021jd035844

Choi, J., Henze, D. K., Wells, K. C., & Millet, D. B. (2025). Joint inversion of Satellite-Based isoprene and formaldehyde observations to constrain emissions of nonmethane volatile organic compounds. *Journal of Geophysical Research Atmospheres*, *130*(13). https://doi.org/10.1029/2024jd042070

Chaliyakunnel, S., Millet, D. B., & Chen, X. (2019). Constraining emissions of volatile organic compounds over the Indian subcontinent using Space-Based formaldehyde measurements. *Journal of Geophysical Research Atmospheres*, *124*(19), 10525–10545. https://doi.org/10.1029/2019jd031262

Chan Miller, C., Jacob, D. J., Marais, E. A., Yu, K., Travis, K. R., Kim, P. S., et al. (2017). Glyoxal yield from isoprene oxidation and relation to formaldehyde: chemical mechanism,

https://doi.org/10.5194/egusphere-2026-6714
Preprint. Discussion started: 17 November 2026
© Author(s) 2026. CC BY 4.0 License.



constraints from SENEX aircraft observations, and interpretation of OMI satellite data. *Atmospheric Chemistry and Physics*, *17*(14), 8725–8738. https://doi.org/10.5194/acp-17-8725-2017

Coggon, M. M., Gkatzelis, G. I., McDonald, B. C., Gilman, J. B., Schwantes, R. H., Abuhassan, N., et al. (2021). Volatile chemical product emissions enhance ozone and modulate urban chemistry. Proceedings of the National Academy of Sciences, 118(32). https://doi.org/10.1073/pnas.2026653118

Coggon, M. M., Stockwell, C. E., Xu, L., Peischl, J., Gilman, J. B., Lamplugh, A., et al. (2024). Contribution of cooking emissions to the urban volatile organic compounds in Las Vegas, NV. *Atmospheric Chemistry and Physics*, *24*(7), 4289–4304. https://doi.org/10.5194/acp-24-4289-2024

Copernicus Sentinel-5P (processed by ESA), 2020. *TROPOMI Level 2 Formaldehyde Total Column products. Version 02.* European Space Agency. https://doi.org/10.5270/S5P-vg1i7t0

Copernicus Sentinel-5P (processed by ESA), 2021. *TROPOMI Level 2 Nitrogen Dioxide total column products. Version 02.* European Space Agency. https://doi.org/10.5270/S5P-9bnp8q8

De Smedt, I., Theys, N., Yu, H., Danckaert, T., Lerot, C., Compernolle, S., et al. (2018). Algorithm theoretical baseline for formaldehyde retrievals from S5P TROPOMI and from the QA4ECV project. *Atmospheric Measurement Techniques*, *11*(4), 2395–2426. https://doi.org/10.5194/amt-11-2395-2018

De Smedt, I., Pinardi, G., Vigouroux, C., Compernolle, S., Bais, A., Benavent, N., et al. (2021). Comparative assessment of TROPOMI and OMI formaldehyde observations and validation against MAX-DOAS network column measurements. *Atmospheric Chemistry and Physics*, *21*(16), 12561–12593. https://doi.org/10.5194/acp-21-12561-2021

Deeter, M., Francis, G., Gille, J., Mao, D., Martínez-Alonso, S., Worden, H., et al. (2022). The MOPITT Version 9 CO product: sampling enhancements and validation. *Atmospheric Measurement Techniques*, *15*(8), 2325–2344. https://doi.org/10.5194/amt-15-2325-2022

DiMaria, C. A., Jones, D. B. A., Worden, H., Bloom, A. A., Bowman, K., Stavrakou, T., et al. (2023). Optimizing the Isoprene emission Model MEGAN with satellite and Ground-Based observational constraints. *Journal of Geophysical Research Atmospheres*, *128*(4). https://doi.org/10.1029/2022jd037822

Dix, B., Li, M., Roosenbrand, E., Francoeur, C., Brown, S. S., Gilman, J. B., et al. (2023).

https://doi.org/10.5194/egusphere-2026-6714
Preprint. Discussion started: 17 November 2026
© Author(s) 2026. CC BY 4.0 License.

Sources of formaldehyde in U.S. oil and gas production regions. *ACS Earth and Space Chemistry*, *7*(12), 2444–2457. https://doi.org/10.1021/acsearthspacechem.3c00203

Doumbia, T., Granier, C., Elguindi, N., Bouarar, I., Darras, S., Brasseur, G., et al. (2021). Changes in global air pollutant emissions during the COVID-19 pandemic: a dataset for atmospheric modeling. *Earth System Science Data*, *13*(8), 4191–4206. https://doi.org/10.5194/essd-13-4191-2021

Feng, S., Jiang, F., Wang, H., Wang, H., Ju, W., Shen, Y., et al. (2020). NO_x Emission Changes Over China During the COVID-19 Epidemic Inferred From Surface NO_2 Observations. *Geophysical Research Letters*, *47*(19). https://doi.org/10.1029/2020gl090080

Feng, S., Jiang, F., Qian, T., Wang, N., Jia, M., Zheng, et al. (2024). Constraining non-methane VOC emissions with TROPOMI HCHO observations: impact on summertime ozone 6simulation in August 2022 in China. *Atmospheric Chemistry and Physics*, *24*(13), 7481–7498. https://doi.org/10.5194/acp-24-7481-2024

Francoeur, C. B., Henze, D. K., He, J., Miller, S. M., Peischl, J., & McDonald, B. C. (2025). Tracking ethane from space over a large US oil and gas region. *Geophysical Research Letters*, *52*(13). https://doi.org/10.1029/2025gl115286

Geng, G., Zhang, Q., Martin, R. V., Lin, J., Huo, H., Zheng, B., et al. (2017). Impact of spatial proxies on the representation of bottom-up emission inventories: A satellite-based analysis. *Atmospheric Chemistry and Physics*, *17*(6), 4131–4145. https://doi.org/10.5194/acp-17-4131-2017

Gaspari, G., & Cohn, S. E. (1999). Construction of correlation functions in two and three dimensions. *Quarterly Journal of the Royal Meteorological Society*, 125(554), 723–757. https://doi.org/10.1002/qj.49712555417

Gaubert, B., Arellano, A. F., Barré, J., Worden, H. M., Emmons, L. K., Tilmes, S., et al. (2016). Toward a chemical reanalysis in a coupled chemistry-climate model: An evaluation of MOPITT CO assimilation and its impact on tropospheric composition. *Journal of Geophysical Research: Atmospheres*, *121*(12), 7310–7343. https://doi.org/10.1002/2016jd024863

Ghahremanloo, M., Nowlan, C., Abad, G. G., Garraffo, C., Liu, X., Wang, H., et al. (2025). Comprehensive Analysis of Bias in TEMPO NO_2 Column Densities through Pandora Observations. *Journal of Geophysical Research Atmospheres*, *130*(15). https://doi.org/10.1029/2025jd044150

Gharamti, M. E., Kershaw, H., Raeder, K., Raczka, B., Johnson, B., Smith, M., et al. (2025).

https://doi.org/10.5194/egusphere-2026-6714
Preprint. Discussion started: 17 November 2026
© Author(s) 2026. CC BY 4.0 License.

The Data Assimilation Research Testbed: A Robust, Scalable Software Facility with Groundbreaking Capabilities for Model-Data Integration. *Bulletin of the American Meteorological Society*, *106*(11), E2328–E2345. https://doi.org/10.1175/bams-d-24-0214.1

Grell, G. A., Peckham, S. E., Schmitz, R., McKeen, S. A., Frost, G., Skamarock, W. C., & Eder, B. (2005). Fully coupled "online" chemistry within the WRF model. *Atmospheric Environment*, 39(37), 6957–6975. https://doi.org/10.1016/j.atmosenv.2005.04.027

González Abad, G., Nowlan, C. R., Liu, X., Wang, H., & Chance, K. (2025). TEMPO Formaldehyde Retrieval Algorithm Theoretical Basis Document. NASA Algorithm Publication Tool, https://doi.org/10.5067/D0GI6E8K0NO8.

Guenther, A. B., Jiang, X., Heald, C. L., Sakulyanontvittaya, T., Duhl, T., Emmons, L. K., & Wang, X. (2012). The Model of Emissions of Gases and Aerosols from Nature version 2.1 (MEGAN2.1): an extended and updated framework for modeling biogenic emissions. *Geoscientific Model Development*, *5*(6), 1471–1492. https://doi.org/10.5194/gmd-5-1471-2012

Goliff, W. S., Stockwell, W. R., & Lawson, C. V. (2012). The regional atmospheric chemistry mechanism, version 2. *Atmospheric Environment*, *68*, 174–185. https://doi.org/10.1016/j.atmosenv.2012.11.038

Hamer, P. D., Bowman, K. W., Henze, D. K., Attié, J., & Marécal, V. (2015). The impact of observing characteristics on the ability to predict ozone under varying polluted photochemical regimes. *Atmospheric Chemistry and Physics*, *15*(18), 10645–10667. https://doi.org/10.5194/acp-15-10645-2015

He, J., Harkins, C., O'Dell, K., Li, M., Francoeur, C., Aikin, K. C., et al. (2023). COVID-19 perturbation on US air quality and human health impact assessment. *PNAS Nexus*, *3*(1), pgad483. https://doi.org/10.1093/pnasnexus/pgad483

Herman, J., Cede, A., Spinei, E., Mount, G., Tzortziou, M., & Abuhassan, N. (2009). NO_2 column amounts from ground-based Pandora and MFDOAS spectrometers using the direct-sun DOAS technique: Intercomparisons and application to OMI validation. *Journal of Geophysical Research Atmospheres*, *114*(D13). https://doi.org/10.1029/2009jd011848

Hong, C., Zhang, Q., He, K., Guan, D., Li, M., Liu, F., et al. (2017). Variations of China's emission estimates: response to uncertainties in energy statistics. *Atmospheric Chemistry and Physics*, *17*(2), 1227–1239. https://doi.org/10.5194/acp-17-1227-2017

Houtekamer, P. L., & Zhang, F. (2016). Review of the Ensemble Kalman Filter for

https://doi.org/10.5194/egusphere-2026-6714
Preprint. Discussion started: 17 November 2026
© Author(s) 2026. CC BY 4.0 License.



Atmospheric Data Assimilation. *Monthly Weather Review*, *144*(12), 4489–4532. https://doi.org/10.1175/mwr-d-15-0440.1

Hsu, C., Henze, D. K., Mizzi, A. P., González Abad, G., He, J., Harkins, C., et al. (2024). An Observing System Simulation Experiment Analysis of How Well Geostationary Satellite Trace-Gas Observations Constrain NO_x Emissions in the US. *Journal of Geophysical Research: Atmospheres*, *129(2)*. https://doi.org/10.1029/2023jd039323

Hsu, C., Henze, D. K., Mizzi, A. P., Harkins, C., Lyu, C., Cooper, O. R., et al. (2026). Top-Down Estimates of U.S. NO_x Emissions Using TEMPO and TROPOMI NO_2 Remote Sensing Observations With WRF-Chem/Chem-DART. *Journal of Geophysical Research Atmospheres*, *131*(2). https://doi.org/10.1029/2025jd044223

Huber, D. E., Kerr, G. H., Nawaz, M. O., Runkel, S., Anenberg, S. C., & Goldberg, D. L. (2026). Global NO_2 changes between 2019 and 2024 as observed by TROPOMI in urban areas and emerging hotspots. *Atmospheric Chemistry and Physics*, *26*(5), 3783–3803. https://doi.org/10.5194/acp-26-3783-2026

Itahashi, S., Yumimoto, K., Kurokawa, J., Morino, Y., Nagashima, T., Miyazaki, K.,et al. (2019). Inverse estimation of NO_x emissions over China and India 2005–2016: contrasting recent trends and future perspectives. *Environmental Research Letters*, *14*(12), 124020. https://doi.org/10.1088/1748-9326/ab4d7f

Janssens-Maenhout, G., Crippa, M., Guizzardi, D., Dentener, F., Muntean, M., Pouliot, G., et al. (2015). HTAP_v2.2: a mosaic of regional and global emission grid maps for 2008 and 2010 to study hemispheric transport of air pollution. *Atmospheric Chemistry and Physics*, *15*(19), 11411–11432. https://doi.org/10.5194/acp-15-11411-2015

Jiang, X., Guenther, A., Potosnak, M., Geron, C., Seco, R., Karl, T., et al. (2018). Isoprene emission response to drought and the impact on global atmospheric chemistry. *Atmospheric Environment*, *183*, 69–83. https://doi.org/10.1016/j.atmosenv.2018.01.026

Jin, X., Fiore, A., Boersma, K. F., De Smedt, I., & Valin, L. (2020). Inferring Changes in Summertime Surface Ozone–NO_x –VOC Chemistry over U.S. Urban Areas from Two Decades of Satellite and Ground-Based Observations. *Environmental Science & Technology*, *54*(11), 6518–6529. https://doi.org/10.1021/acs.est.9b07785

Jin, X., Yang, Y., Abad, G. G., Nowlan, C., & Liu, X. (2025). Observing the Diurnal Variations of Ozone-NO_x-VOC Chemistry Over the U.S. From the Geostationary TEMPO Instrument. *Geophysical Research Letters*, *52*(14). https://doi.org/10.1029/2025gl116394

Jung, J., Choi, Y., Mousavinezhad, S., Kang, D., Park, J., Pouyaei, A., et al. (2022). Changes

https://doi.org/10.5194/egusphere-2026-6714
Preprint. Discussion started: 17 November 2026
© Author(s) 2026. CC BY 4.0 License.

in the ozone chemical regime over the contiguous United States inferred by the inversion of NO_x and VOC emissions using satellite observation. *Atmospheric Research*, *270*, 106076. https://doi.org/10.1016/j.atmosres.2022.106076

Judd, L. M., Al-Saadi, J. A., Szykman, J. J., Valin, L. C., Janz, S. J., Kowalewski, et al. (2020). Evaluating Sentinel-5P TROPOMI tropospheric NO_2 column densities with airborne and Pandora spectrometers near New York City and Long Island Sound. *Atmospheric Measurement Techniques*, *13*(11), 6113–6140. https://doi.org/10.5194/amt-13-6113-2020

Kang, J., Kalnay, E., Liu, J., Fung, I., Miyoshi, T., & Ide, K. (2011). "Variable localization" in an ensemble Kalman filter: Application to the carbon cycle data assimilation. *Journal of Geophysical Research Atmospheres*, *116*(D9). https://doi.org/10.1029/2010jd014673

Kaiser, J., Jacob, D. J., Zhu, L., Travis, K. R., Fisher, J. A., Abad, G. G., et al. (2018). High-resolution inversion of OMI formaldehyde columns to quantify isoprene emission on ecosystem-relevant scales: application to the southeast US. *Atmospheric Chemistry and Physics*, *18*(8), 5483–5497. https://doi.org/10.5194/acp-18-5483-2018

Kim, J., Jeong, U., Ahn, M., Kim, J. H., Park, R. J., Lee, H., et al. (2019). New Era of Air Quality Monitoring from Space: Geostationary Environment Monitoring Spectrometer (GEMS). *Bulletin of the American Meteorological Society*, *101*(1), E1–E22. https://doi.org/10.1175/bams-d-18-0013.1

Knighton, W. B., Herndon, S. C., Franklin, J. F., Wood, E. C., Wormhoudt, J., Brooks, W., et al. (2012). Direct measurement of volatile organic compound emissions from industrial flares using real-time online techniques: Proton Transfer Reaction Mass Spectrometry and Tunable Infrared Laser Differential Absorption Spectroscopy. *Industrial & Engineering Chemistry Research*, *51*(39), 12674–12684. https://doi.org/10.1021/ie202695v

Kong, L., Tang, X., Wang, Z., Zhu, J., Li, J., Wu, H., et al. (2024). Changes in air pollutant emissions in China during two clean-air action periods derived from the newly developed Inversed Emission Inventory for Chinese Air Quality (CAQIEI). *Earth System Science Data*, *16*(9), 4351–4387. https://doi.org/10.5194/essd-16-4351-2024

Lamsal, L. N., Martin, R. V., Van Donkelaar, A., Steinbacher, M., Celarier, E. A., Bucsela, E., Dunlea, E. J., & Pinto, J. P. (2008). Ground-level nitrogen dioxide concentrations inferred from the satellite-borne Ozone Monitoring Instrument. *Journal of Geophysical Research Atmospheres*, *113*(D16). https://doi.org/10.1029/2007jd009235

Lange, K., Richter, A., Schönhardt, A., Meier, A. C., Bösch, T., Seyler, A., et al. (2023). Validation of Sentinel-5P TROPOMI tropospheric NO_2 products by comparison with NO_2

https://doi.org/10.5194/egusphere-2026-6714
Preprint. Discussion started: 17 November 2026
© Author(s) 2026. CC BY 4.0 License.

measurements from airborne imaging DOAS, ground-based stationary DOAS, and mobile car DOAS measurements during the S5P-VAL-DE-Ruhr campaign. *Atmospheric Measurement Techniques*, *16*(5), 1357–1389. https://doi.org/10.5194/amt-16-1357-2023

Lelieveld, J., Evans, J. S., Fnais, M., Giannadaki, D., & Pozzer, A. (2015). The contribution of outdoor air pollution sources to premature mortality on a global scale. *Nature*, *525*(7569), 367–371. https://doi.org/10.1038/nature15371

Lerner, B. M., Gilman, J. B., Aikin, K. C., Atlas, E. L., Goldan, P. D., Graus, M., et al. (2017). An improved, automated whole air sampler and gas chromatography mass spectrometry analysis system for volatile organic compounds in the atmosphere. *Atmospheric Measurement Techniques*, *10*(1), 291–313. https://doi.org/10.5194/amt-10-291-2017

Li, F., Zhang, X., Kondragunta, S., Lu, X., Csiszar, I., & Schmidt, C. C. (2022). Hourly biomass burning emissions product from blended geostationary and polar-orbiting satellites for air quality forecasting applications. *Remote Sensing of Environment*, *281*, 113237. https://doi.org/10.1016/j.rse.2022.113237

Liu, X. (2026a). *TEMPO NO2 tropospheric and stratospheric columns V04 (PROVISIONAL)* [Dataset]. NASA Langley Atmospheric Science Data Center Distributed Active Archive Center. https://doi.org/10.5067/IS-40E/TEMPO/NO2_L2.004

Liu, X. (2026b). *TEMPO formaldehyde total column V04 (PROVISIONAL)* [Dataset]. NASA Langley Atmospheric Science Data Center Distributed Active Archive Center. https://doi.org/10.5067/IS-40E/TEMPO/HCHO_L2.004

Lyu, C., Harkins, C., Li, M., Mueller, K., Prothero, J., Verreyken, B., et al. (2025). Development of the United States GReenhouse gas and Air Pollutants Emissions System (GRA2PES). Journal of Geophysical Research: Atmospheres, 130, e2025JD043597. https://doi.org/10.1029/2025JD043597

Ma, C., Wang, T., Mizzi, A. P., Anderson, J. L., Zhuang, B., Xie, M., & Wu, R. (2019). Multiconstituent Data Assimilation With WRF-Chem/DART: Potential for Adjusting Anthropogenic Emissions and Improving Air Quality Forecasts Over Eastern China. *Journal of Geophysical Research: Atmospheres*, https://doi.org/10.1029/2019jd030421

Mao, J., Carlton, A., Cohen, R. C., Brune, W. H., Brown, S. S., Wolfe, G. M., et al. (2018). Southeast Atmosphere Studies: learning from model-observation syntheses. *Atmospheric Chemistry and Physics*, *18*(4), 2615–2651. https://doi.org/10.5194/acp-18-2615-2018

McDonald, B. C., De Gouw, J. A., Gilman, J. B., Jathar, S. H., Akherati, A., Cappa, C. D., et al. (2018). Volatile chemical products emerging as largest petrochemical source of urban

https://doi.org/10.5194/egusphere-2026-6714
Preprint. Discussion started: 17 November 2026
© Author(s) 2026. CC BY 4.0 License.



organic emissions. *Science*, *359*(6377), 760–764. https://doi.org/10.1126/science.aaq0524

Min, K., Washenfelder, R. A., Dubé, W. P., Langford, A. O., Edwards, P. M., Zarzana, K. J., et al. (2016). A broadband cavity enhanced absorption spectrometer for aircraft measurements of glyoxal, methylglyoxal, nitrous acid, nitrogen dioxide, and water vapor. *Atmospheric Measurement Techniques*, *9*(2), 423–440. https://doi.org/10.5194/amt-9-423-2016

Millet, D. B., Palmer, P. I., Levelt, P. F., Gallardo, L., & Shikwambana, L. (2024). Coordinated geostationary, multispectral satellite observations are critical for climate and air quality progress. *AGU Advances*, *5*(5). https://doi.org/10.1029/2024av001322

Miyazaki, K., Eskes, H., Sudo, K., Boersma, K. F., Bowman, K., & Kanaya, Y. (2017). Decadal changes in global surface NO_x emissions from multi-constituent satellite data assimilation. *Atmospheric Chemistry and Physics*, *17*(2), 807–837. https://doi.org/10.5194/acp-17-807-2017

Miyazaki, K., Bowman, K., Sekiya, T., Eskes, H., Boersma, F., Worden, H., et al. (2020). Updated tropospheric chemistry reanalysis and emission estimates, TCR-2, for 2005–2018. *Earth System Science Data*, *12*(3), 2223–2259. https://doi.org/10.5194/essd-12-2223-2020

Mizzi, A. P., Arellano Jr., A. F., Edwards, D. P., Anderson, J. L., & Pfister, G. G. (2016). Assimilating compact phase space retrievals of atmospheric composition with WRF-Chem/DART: a regional chemical transport/ensemble Kalman filter data assimilation system. *Geoscientific Model Development*, *9(3)*, 965–978. https://doi.org/10.5194/gmd-9-965-2016

Mizzi, A. P., Edwards, D. P., & Anderson, J. L. (2018). Assimilating compact phase space retrievals (CPSRs): comparison with independent observations (MOZAIC in situ and IASI retrievals) and extension to assimilation of truncated retrieval profiles. *Geoscientific Model Development*, *11(9)*, 3727–3745. https://doi.org/10.5194/gmd-11-3727-2018

Moon, J., Jeon, W., Jeong, S., Choi, Y., Kim, H. C., Park, S., et al. (2026). Spatiotemporal optimization of NO_x and VOC emissions using a hybrid inversion framework and implications for ozone sensitivity-regime diagnosis. *Atmospheric Chemistry and Physics*, *26*(14), 10379–10398. https://doi.org/10.5194/acp-26-10379-2026

Mouat, A. P., Siegel, Z. A., & Kaiser, J. (2024). Evaluation of Aeris mid-infrared absorption (MIRA), Picarro CRDS (cavity ring-down spectroscopy) G2307, and

https://doi.org/10.5194/egusphere-2026-6714
Preprint. Discussion started: 17 November 2026
© Author(s) 2026. CC BY 4.0 License.

dinitrophenylhydrazine (DNPH)-based sampling for long-term formaldehyde monitoring efforts. *Atmospheric Measurement Techniques*, *17*(7), 1979–1994. https://doi.org/10.5194/amt-17-1979-2024

Nowlan, C. R., Abad, G. G., Kwon, H., Ayazpour, Z., Miller, C. C., Chance, K., et al. (2023). Global formaldehyde products from the Ozone Mapping and Profiler Suite (OMPS) Nadir Mappers on Suomi NPP and NOAA-20. *Earth and Space Science*, *10*(5). https://doi.org/10.1029/2022ea002643

Nowlan, C., González Abad, G., Liu X., Wang, H., and Chance, K. (2025). *TEMPO Nitrogen Dioxide Retrieval Algorithm Theoretical Basis Document*. https://doi.org/10.5067/WX026254FI2U

Oomen, G. M., Müller, J. F., Stavrakou, T., De Smedt, I., Blumenstock, T., Kivi, R., et al. (2024). Weekly derived top-down volatile-organic-compound fluxes over Europe from TROPOMI HCHO data from 2018 to 2021. *Atmospheric Chemistry and Physics*, *24*(1), 449–474. https://doi.org/10.5194/acp-24-449-2024

Oomen, G., Choi, J., Yu, J., Miyazaki, K., Arellano, A. F. J., Stavrakou, et al. (2026). Improved determination of atmospheric trace gas emissions through observation-based analysis techniques: The AMIGO global initiative. *Elementa Science of the Anthropocene*, *14*(1). https://doi.org/10.1525/elementa.2025.00092

Opacka, B., Stavrakou, T., Müller, J., De Smedt, I., Van Geffen, J., Marais, E. A., et al. (2025). Natural emissions of VOC and NO_x over Africa constrained by TROPOMI HCHO and NO_2 data using the MAGRITTEv1.1 model. *Atmospheric Chemistry and Physics*, *25*(5), 2863–2894. https://doi.org/10.5194/acp-25-2863-2025

Ortega, I., Hannigan, J. W., Edwards, D., Stremme, W., Grutter, M., Cadena-Caicedo, A., et al. (2026). Evaluating TEMPO formaldehyde retrievals with Co-Located Ground-Based FTIR and Pandora observations. *Journal of Geophysical Research Atmospheres*, *131*(9). https://doi.org/10.1029/2026jd046497

Pierce, T., Geron, C., Bender, L., Dennis, R., Tonnesen, G., & Guenther, A. (1998). Influence of increased isoprene emissions on regional ozone modeling. *Journal of Geophysical Research Atmospheres*, *103*(D19), 25611–25629. https://doi.org/10.1029/98jd01804

Qu, Z., Henze, D. K., Worden, H. M., Jiang, Z., Gaubert, B., Theys, N., & Wang, W. (2022). Sector-Based Top-Down Estimates of NO_x, SO_2, and CO Emissions in East Asia. *Geophysical Research Letters*, *49*(2). https://doi.org/10.1029/2021gl096009

Rawat, P., Crawford, J. H., Travis, K. R., Judd, L. M., Demetillo, M. a. G., Valin, L. C., et al.

https://doi.org/10.5194/egusphere-2026-6714
Preprint. Discussion started: 17 November 2026
© Author(s) 2026. CC BY 4.0 License.

(2025). Maximizing the scientific application of Pandora column observations of HCHO and NO_2. *Atmospheric Measurement Techniques*, *18*(13), 2899–2917. https://doi.org/10.5194/amt-18-2899-2025

Rawat, P., Travis, K. R., Henderson, B., Crawford, J. H., Judd, L. M., Demetillo, M. a. G., et al. (2026). Spatiotemporal assessment of the TEMPO formaldehyde column retrieval using the Pandonia Global Network. *Journal of Geophysical Research Atmospheres*, *131*(2). https://doi.org/10.1029/2025jd044788

Rollins, A. W., Rickly, P. S., Gao, R., Ryerson, T. B., Brown, S. S., Peischl, J., et al. (2020). Single-photon laser-induced fluorescence detection of nitric oxide at sub-parts-per-trillion mixing ratios. *Atmospheric Measurement Techniques*, *13*(5), 2425–2439. https://doi.org/10.5194/amt-13-2425-2020

Seinfeld, J. H., & Pandis, S. N. (2012). *Atmospheric Chemistry and Physics*. John Wiley & Sons.

Seco, R., Holst, T., Davie-Martin, C. L., Simin, T., Guenther, A., Pirk, N., et al. (2022). Strong isoprene emission response to temperature in tundra vegetation. *Proceedings of the National Academy of Sciences*, *119*(38). https://doi.org/10.1073/pnas.2118014119

Sekiya, T., Miyazaki, K., Ogochi, K., Sudo, K., Takigawa, M., Eskes, H., et al. (2021). Impacts of horizontal resolution on global data Assimilation of satellite measurements for tropospheric chemistry analysis. *Journal of Advances in Modeling Earth Systems*, *13*(6). https://doi.org/10.1029/2020ms002180

Simon, H., Hogrefe, C., Whitehill, A., Foley, K. M., Liljegren, J., Possiel, N., et al. (2024). Revisiting day-of-week ozone patterns in an era of evolving US air quality. *Atmospheric Chemistry and Physics*, *24*(3), 1855–1871. https://doi.org/10.5194/acp-24-1855-2024

Skipper, T. N., D'Ambro, E. L., Wiser, F. C., McNeill, V. F., Schwantes, R. H., Henderson, B. et al. (2024). Role of chemical production and depositional losses on formaldehyde in the Community Regional Atmospheric Chemistry Multiphase Mechanism (CRACMM). *Atmospheric Chemistry and Physics*, *24*(22), 12903–12924. https://doi.org/10.5194/acp-24-12903-2024

Solazzo, E., Bianconi, R., Hogrefe, C., Curci, G., Tuccella, P., Alyuz, U., et al. (2017). Evaluation and error apportionment of an ensemble of atmospheric chemistry transport modeling systems: multivariable temporal and spatial breakdown. *Atmospheric Chemistry and Physics*, *17*(4), 3001–3054. https://doi.org/10.5194/acp-17-3001-2017

Souri, A. H., Nowlan, C. R., González Abad, G., Zhu, L., Blake, D. R., Fried, A., et al. (2020).

https://doi.org/10.5194/egusphere-2026-6714
Preprint. Discussion started: 17 November 2026
© Author(s) 2026. CC BY 4.0 License.

An inversion of NO_x and non-methane volatile organic compound (NMVOC) emissions using satellite observations during the KORUS-AQ campaign and implications for surface ozone over East Asia. *Atmospheric Chemistry and Physics*, *20*(16), 9837–9854. https://doi.org/10.5194/acp-20-9837-2020

Spinei, E., Whitehill, A., Fried, A., Tiefengraber, M., Knepp, T. N., Herndon, S., et al. (2018). The first evaluation of formaldehyde column observations by improved Pandora spectrometers during the KORUS-AQ field study. *Atmospheric Measurement Techniques*, *11*(9), 4943–4961. https://doi.org/10.5194/amt-11-4943-2018

Stanier, C. O., Pierce, R. B., Abdi-Oskouei, M., Adelman, Z. E., Al-Saadi, J., Alwe, H. D., et al. (2021). Overview of the Lake Michigan Ozone Study 2017. *Bulletin of the American Meteorological Society*, *102*(12), E2207–E2225. https://doi.org/10.1175/bams-d-20-0061.1

Stavrakou, T., Müller, J. F., De Smedt, I., Van Roozendael, M., van der Werf, G. R., Giglio, L., & Guenther, A. (2009). Global emissions of non-methane hydrocarbons deduced from SCIAMACHY formaldehyde columns through 2003–2006. *Atmospheric Chemistry and Physics*, *9*(11), 3663–3679. https://doi.org/10.5194/acp-9-3663-2009

Stockwell, C. E., Bela, M. M., Coggon, M. M., Gkatzelis, G. I., Wiggins, E., Gargulinski, E. M., et al. (2022). Airborne emission rate measurements validate remote sensing observations and emission inventories of western U.S. wildfires. *Environmental Science & Technology*, *56*(12), 7564–7577. https://doi.org/10.1021/acs.est.1c07121

Sun, K., Saju, J. A., Nowlan, C. R., Abad, G. G., & Liu, X. (2025). Hourly nitrogen oxides emissions estimated from TEMPO and comparison with Facility-Level monitoring data. *Journal of Geophysical Research Atmospheres*, *130*(23). https://doi.org/10.1029/2025jd044565

Tippett, M. K., Anderson, J. L., Bishop, C. H., Hamill, T. M., & Whitaker, J. S. (2003). Ensemble Square Root Filters. *Monthly Weather Review*, *131*(7), 1485–1490. https://doi.org/10.1175/1520-0493(2003)131

Travis, K. R., Jacob, D. J., Fisher, J. A., Kim, P. S., Marais, E. A., Zhu, L., et al. (2016). Why do models overestimate surface ozone in the Southeast United States? *Atmospheric Chemistry and Physics*, *16*(21), 13561–13577. https://doi.org/10.5194/acp-16-13561-2016

Turner, M. C., Jerrett, M., Pope, C. A., Krewski, D., Gapstur, S. M., Diver, W. R., et al. (2015). Long-Term ozone exposure and mortality in a large prospective study. *American Journal*

https://doi.org/10.5194/egusphere-2026-6714
Preprint. Discussion started: 17 November 2026
© Author(s) 2026. CC BY 4.0 License.



of Respiratory and Critical Care Medicine, *193*(10), 1134–1142. https://doi.org/10.1164/rccm.201508-1633oc

Verhoelst, T., Compernolle, S., Pinardi, G., Lambert, J., Eskes, H. J., Eichmann, K., et al. (2021). Ground-based validation of the Copernicus Sentinel-5P TROPOMI NO2 measurements with the NDACC ZSL-DOAS, MAX-DOAS and Pandonia global networks. *Atmospheric Measurement Techniques*, *14*(1), 481–510. https://doi.org/10.5194/amt-14-481-2021

Vigouroux, C., Langerock, B., Bauer Aquino, C. A., Blumenstock, T., Cheng, Z., De Mazière, M., et al. (2020). TROPOMI–Sentinel-5 Precursor formaldehyde validation using an extensive network of ground-based Fourier-transform infrared stations. *Atmospheric Measurement Techniques*, *13*(7), 3751–3767. https://doi.org/10.5194/amt-13-3751-2020

Walker, J. C., Dudhia, A., & Carboni, E. (2011). An effective method for the detection of trace species demonstrated using the MetOp Infrared Atmospheric Sounding Interferometer. *Atmospheric Measurement Techniques*, *4*(8), 1567–1580. https://doi.org/10.5194/amt-4-1567-2011

Warneke, C., De Gouw, J. A., Del Negro, L., Brioude, J., McKeen, S., Stark, H., et al. (2010). Biogenic emission measurement and inventories determination of biogenic emissions in the eastern United States and Texas and comparison with biogenic emission inventories. *Journal of Geophysical Research Atmospheres*, *115*(D7). https://doi.org/10.1029/2009jd012445

Waxman, E. M., Gao, R., Thornberry, T., McLaughlin, R., Novak, G., Atlas, E., et al. (2025). Observationally Constrained NO_x-Catalyzed Ozone Production in the Upper Troposphere During the Asian Summer Monsoon. *Journal of Geophysical Research Atmospheres*, *130*(19). https://doi.org/10.1029/2024jd043218

Wells, K. C., Millet, D. B., Payne, V. H., Deventer, M. J., Bates, K. H., de Gouw, J. A., et al. (2020). Satellite isoprene retrievals constrain emissions and atmospheric oxidation. *Nature*, *585*(7824), 225–233. https://doi.org/10.1038/s41586-020-2664-3

Wells, K. C., Millet, D. B., Payne, V. H., Vigouroux, C., Aquino, C. a. B., De Mazière, M., et al. (2022). Next-Generation Isoprene Measurements from Space: detecting daily variability at high resolution. *Journal of Geophysical Research Atmospheres*, *127*(5). https://doi.org/10.1029/2021jd036181

Wells, K. C., Millet, D. B., Brewer, J. F., Payne, V. H., Cady-Pereira, K. E., Pernak, R., et al. (2025). Global decadal measurements of methanol, ethene, ethyne, and HCN from the

https://doi.org/10.5194/egusphere-2026-6714
Preprint. Discussion started: 17 November 2026
© Author(s) 2026. CC BY 4.0 License.

Cross-track Infrared Sounder. *Atmospheric Measurement Techniques*, *18*(3), 695–716. https://doi.org/10.5194/amt-18-695-2025

Wells, K. C., Millet, D. B., Brewer, J. F., Payne, V. H., Cady-Pereira, K. E., Pernak, R., et al. (2025). Global decadal measurements of methanol, ethene, ethyne, and HCN from the Cross-track Infrared Sounder. *Atmospheric Measurement Techniques*, *18*(3), 695–716. https://doi.org/10.5194/amt-18-695-2025

World Health Organization. (2021). WHO global air quality guidelines: Particulate matter ($PM_{2.5}$ and PM_{10}), ozone, nitrogen dioxide, sulfur dioxide and carbon monoxide. World Health Organization. https://www.who.int/publications/i/item/9789240034228

Wolfe, G. M., Kaiser, J., Hanisco, T. F., Keutsch, F. N., De Gouw, J. A., Gilman, J. B., et al. (2016). Formaldehyde production from isoprene oxidation across NO_x regimes. *Atmospheric Chemistry and Physics*, *16*(4), 2597–2610. https://doi.org/10.5194/acp-16-2597-2016

Wu, H., Kong, L., Tang, X., Zhu, L., Zhu, J., & Wang, Z. (2023). Air Quality Forecasting with Inversely Updated Emissions for China. *Environmental Science & Technology Letters*, *10*(8), 655–661. https://doi.org/10.1021/acs.estlett.3c00266

Yuan, B., Koss, A., Warneke, C., Gilman, J. B., Lerner, B. M., Stark, H., et al. (2016). A high-resolution time-of-flight chemical ionization mass spectrometer utilizing hydronium ions (H_3O^+ ToF-CIMS) for measurements of volatile organic compounds in the atmosphere. *Atmospheric Measurement Techniques*, *9*(6), 2735–2752. https://doi.org/10.5194/amt-9-2735-2016

Yu, K. A., Li, M., Harkins, C., He, J., Zhu, Q., Verreyken, B., et al. (2023). Improved spatial resolution in modeling of nitrogen oxide concentrations in the Los Angeles Basin. *Environmental Science & Technology*, *57*(49), 20689–20698. https://doi.org/10.1021/acs.est.3c06158

Zare, A., Romer, P. S., Nguyen, T., Keutsch, F. N., Skog, K., & Cohen, R. C. (2018). A comprehensive organic nitrate chemistry: insights into the lifetime of atmospheric organic nitrates. *Atmospheric Chemistry and Physics*, *18*(20), 15419–15436. https://doi.org/10.5194/acp-18-15419-2018

Zhu, Q., Laughner, J. L., & Cohen, R. C. (2022). Estimate of OH trends over one decade in North American cities. *Proceedings of the National Academy of Sciences*, *119*(16), e2117399119. https://doi.org/10.1073/pnas.2117399119

Zhu, Q., Schwantes, R. H., Coggon, M., Harkins, C., Schnell, J., He, J., et al. (2024). A better

https://doi.org/10.5194/egusphere-2026-6714
Preprint. Discussion started: 17 November 2026
© Author(s) 2026. CC BY 4.0 License.



representation of volatile organic compound chemistry in WRF-Chem and its impact on ozone over Los Angeles. *Atmospheric Chemistry and Physics*, *24*(9), 5265–5286. https://doi.org/10.5194/acp-24-5265-2024

Zhu, Q., Schwantes, R. H., Stockwell, C. E., Harkins, C., Lyu, C., Coggon, M., et al. (2025). Incorporating cooking emissions to better simulate the impact of Zero-Emission vehicle adoption on ozone pollution in Los Angeles. *Environmental Science & Technology*, *59*(11), 5672–5682. https://doi.org/10.1021/acs.est.5c00902

Zoogman, P., Liu, X., Suleiman, R., Pennington, W., Flittner, D., Al-Saadi, J., et al. (2016). Tropospheric emissions: Monitoring of pollution (TEMPO). *Journal of Quantitative Spectroscopy and Radiative Transfer*, *186*, 17–39. https://doi.org/10.1016/j.jqsrt.2016.05.008